Characterizing Microbubble-Mediated Permeabilization in a Vessel-on-a-Chip Model

Meijlink, Bram; Collado-Lara, Gonzalo; Bishard, Kristina; Conboy, James P.; Langeveld, Simone A.G.; Koenderink, Gijsje H.; van der Steen, Antonius F.W.; de Jong, Nico; Kooiman, Klazina; More Authors

DOI
10.1002/smll.202407550

Publication date
2024

Document Version
Final published version

Published in
Small

Citation (APA)
Meijlink, B., Collado-Lara, G., Bishard, K., Conboy, J. P., Langeveld, S. A. G., Koenderink, G. H., van der Steen, A. F. W., de Jong, N., Kooiman, K., & More Authors (2024). Characterizing Microbubble-Mediated Permeabilization in a Vessel-on-a-Chip Model. *Small*, *21*(4), Article 2407550. https://doi.org/10.1002/smll.202407550

NANO · MICRO small
www.small-journal.com

Characterizing Microbubble-Mediated Permeabilization in a Vessel-on-a-Chip Model

*Bram Meijlink, Gonzalo Collado-Lara, Kristina Bishard, James P. Conboy, Simone A.G. Langeveld, Gijsje H. Koenderink, Antonius F. W. van der Steen, Nico de Jong, Inés Beekers, Sebastiaan J. Trietsch, and Klazina Kooiman**

Drug transport from blood to extravascular tissue can locally be achieved by increasing the vascular permeability through ultrasound-activated microbubbles. However, the mechanism remains unknown, including whether short and long cycles of ultrasound induce the same onset rate, spatial distribution, and amount of vascular permeability increase. Accurate models are necessary for insights into the mechanism so a microvessel-on-a-chip is developed with a membrane-free extravascular space. Using these microvessels-on-a-chip, distinct differences between 2 MHz ultrasound treatments are shown with 10 or 1000 cycles. The onset rate is slower for 10 than 1000 cycles, while both cycle lengths increase the permeability in spot-wise patterns without affecting microvessel viability. Significantly less vascular permeability increase and sonoporation are induced for 10 versus 1000 cycles at 750 kPa (i.e., the highest studied peak negative acoustic pressure (PNP)). The PNP threshold for vascular permeability increases is 750 versus 550 kPa for 10 versus 1000 cycles, while this is 750 versus 220 kPa for sonoporation. Vascular permeability increases do not correlate with $\alpha_v\beta_3$-targeted microbubble behavior, while sonoporation correlates with $\alpha_v\beta_3$-targeted microbubble clustering. In conclusion, the further mechanistic unraveling of vascular permeability increase by ultrasound-activated microbubbles in a developed microvessel-on-a-chip model aids the safe and efficient development of microbubble-mediated drug transport.

1. Introduction

The vessel wall is an important barrier for the successful delivery of drugs to the underlying diseased tissue. An impermeable vascular wall caused by, for example, the blood-brain barrier, or as a result of anti-angiogenic treatment for non-brain cancer, hinders the extravasation of pharmacological agents and thus reduces treatment efficiency.[1–3] A potential way to increase treatment efficiency and reduce side effects is to locally enhance vascular permeability using lipid-coated gas microbubbles (MBs) of 1–10 µm in diameter in combination with an ultrasound.[4,5]

MBs have clinically been used as a contrast agent for diagnostic ultrasound imaging for several decades.[6,7] Previous research has also shown that the expansion, contraction, and collapse of MBs by ultrasound can induce multiple vascular drug delivery pathways, such as sonoporation (onset within ms), tunnel formation (onset within ms), cell-cell contact opening (onset within 15 s), (onset within min) and endocytosis.[8–11] Sonoporation and endocytosis result in intracellular drug uptake induced by the mechanical stresses following MB oscillations close to a cell.[10,12] In addition, sonoporation increases intracellular calcium,[9,13–15] which correlated with cell-cell contact opening.[16] As a result of oscillating MBs, the formation of an apical-to-basal tunnel through the cell has recently been reported.[17,18] Cell–cell contact opening and tunnel formation could potentially induce

B. Meijlink, G. Collado-Lara, S. A. Langeveld, A. F. W. van der Steen, N. de Jong, I. Beekers, K. Kooiman
Biomedical Engineering
Department of Cardiology
Cardiovascular Institute
Erasmus MC
Wytemaweg 80, Rotterdam 3015 CN, The Netherlands
E-mail: k.kooiman@erasmusmc.nl

The ORCID identification number(s) for the author(s) of this article can be found under https://doi.org/10.1002/smll.202407550

DOI: 10.1002/smll.202407550

K. Bishard, S. J. Trietsch
Mimetas B.V.
De Limes 7, Oegstgeest 2342 DH, The Netherlands

J. P. Conboy, G. H. Koenderink
Department of Bionanoscience
Delft University of Technology
Building 58, Van der Maasweg 9, Delft 2629 HZ, The Netherlands

A. F. W. van der Steen, N. de Jong
Department of Imaging Physics
Delft University of Technology
Building 22, Lorentzweg 1, Delft 2628 CJ, The Netherlands

I. Beekers
Department of Health
ORTEC B.V.
Houtsingel 5, Zoetermeer 2719 EA, The Netherlands

transcellular and paracellular transportation of molecules over the endothelial layer, resulting in local MB-mediated vascular permeability increase. Investigations into vascular permeability increases by oscillating MBs are mainly studied in animal models, where both short 5[19] and 10 cycles[20,21] and longer 100,[22] 5000[21] and 10 000[19,23] cycles have shown to increase vascular permeability. However, an in vitro model in which the effect of short and long cycles on the onset rate, spatial distribution, and amount of vascular permeability increase can be investigated is lacking. Having the means to compare these parameters in an in vitro model will improve assay controllability and scalability while reducing the ethical concerns of in vivo experiments. At the same time, the reported clinical study on increasing chemotherapy delivery by oscillating MBs for pancreatic cancer used 4 cycles.[24] The reason for this short cycle is the fixed number of cycles in clinical ultrasound machines.[25] This is another reason why MB-cell-drug interactions translating to vascular permeability changes need to be investigated for both short and long cycles so maximum therapeutic outcome and widespread clinical use can be achieved.

Accurate models are necessary to provide insights into the mechanism of microbubble-mediated drug delivery, thereby enabling safety and controllability. Up to now, in vitro research on MB-mediated vascular drug delivery pathways has been performed almost exclusively on 2D endothelial cell models, in which cells are grown in a monolayer on a glass or membrane substrate.[26] Consequently, it is challenging to investigate the transportation of molecules beyond the endothelial layer in the current 2D models. Moreover, 2D models usually use static growth conditions while it has been shown that growing endothelial cells under flow affects sonoporation and calcium fluxes.[27] MB-mediated transportation of molecules beyond the endothelial layer under flow conditions has been investigated optically in vivo using chicken embryo[20] and dorsal window mice models.[23] While animal models can provide more accuracy, they raise ethical concerns, have a lower throughput than in vitro models and the differences between animals limit the controllability of the model. These considerations emphasize the need for an advanced in vitro model with physiologically relevant cell behavior to investigate MB-mediated vascular permeability changes.

Microvessel-on-a-chip models are advanced in vitro models in which 3D artificial blood vessels are grown under flow.[28] For this reason, they are more physiologically relevant than in vitro 2D monolayers. At the same time, they provide a higher throughput with fewer ethical objections than in vivo models. Two recent studies showed the feasibility of using vessel-on-a-chip models to gain insight into microbubble-mediated sonoporation under flow[29] and the induction of cell–cell contact gaps.[30] However, both these models still contained a membrane, meaning vascular permeability could not be investigated. The OrganoPlate 3-lane 40 (4003-400-B, Mimetas, Leiden, NL) is a commercially available organ-on-a-chip model in which an advanced membrane-free 3D microvessel can be grown under flow alongside an extravascular space.[31,32] Tissue in this plate can be cultured under flow created via gravity-driven medium recirculation perfusion by tilting the OrganoPlate at predetermined angles and intervals using the OrganoFlow rocking platform. Acoustic characterization of the OrganoPlate indicated that controlled MB behavior can be achieved within the chips.[33] These properties make the microvessel-on-a-chip grown in the OrganoPlate a promising model to investigate vascular permeability and how this permeability is affected by MB and ultrasound treatment.

In this study, we developed a microvessel-on-a-chip model with a perfusable lumen and extravascular space in the OrganoPlate 3-lane with the aim to investigate ultrasound and $\alpha_v\beta_3$-targeted MB ($\alpha_v\beta_3$-tMB) mediated changes in vascular permeability and sonoporation. The tMBs were selected based on their significantly better therapeutic outcome than non-tMBs both in vitro and preclinically in vivo.[34] In addition, the integrin $\alpha_v\beta_3$ is a clinically relevant endothelial biomarker as it is expressed during angiogenesis in both cancer and atherosclerosis.[9] At five different acoustic peak negative pressures (90–750 kPa), we investigated 10 cycle as well as 1000 cycle pulses at an ultrasound frequency of 2 MHz. At the lowest acoustic pressure mainly stable cavitation is expected, while for the highest pressure inertial cavitation will be dominant. Based on previous publications both the short 10 cycle[8,9,20] and long 1000 cycle pulses[29,35,36] will induce sonoporation, cell–cell-contact opening, and vascular permeability in vitro and in vivo. The applied pulses were repeated 10 times since pulse repetitions have been shown to enhance vascular permeability in vivo.[23] Using real-time microscopy, $\alpha_v\beta_3$-tMBs dynamics were recorded, vascular permeability was investigated for 2 h with a barrier integrity (BI) assay and sonoporation was investigated with the model drug propidium iodide. From these microscopy studies, the onset rate and spatial distribution of the vascular permeability increase were determined and correlated to MB dynamics and sonoporation. The effect of the MB and ultrasound treatment on the cell viability in the microvessel was assessed using a WST-8 colorimetric assay which measures metabolic activity.

2. Results and Discussion

2.1. Establishing the Microvessel-on-a-Chip Model

The microfluidic OrganoPlate 3-lane 40 platform (**Figure 1A**) was used to grow a 3D microvessel-on-a-chip model (Figure 1B). To achieve a membrane-free configuration between the cellular layer and extravascular space, collagen I extracellular matrix (ECM) gel was used. Depending on the lot numbers (n = 3), the median Young's modulus of the gel measured between 0.43 and 0.68 kPa (Figure S1, Supporting Information). These values are within previously reported basal membrane ranges for endothelial cells (0.5–1 kPa)[37] and orders of magnitude lower than the reported GPa Young's modulus for polymer membranes, plastics, glass, or human bone.[38,39] The observed 1.6 fold differences between the lot numbers could be a result of variation during the isolation of the collagen by the supplier, or be due to temperature differences during the neutralization and seeding of the gel.[40]

Microvessel culture was performed based on a previous publication.[41] In short, microvessel growth started by dispensing the ECM gel into the middle channel (Figure 1C). Following gel loading, human dermal microvascular endothelial cells (HMEC-1) were seeded and incubated under a 105° angle as per instruction of the manufacturer to attach the cells to the gel layer. The microvessel formation within the vessel channel over a 4-day time period, in which the cells were cultured under bidirectional flow, is shown in Figure 1C. Using this method, a

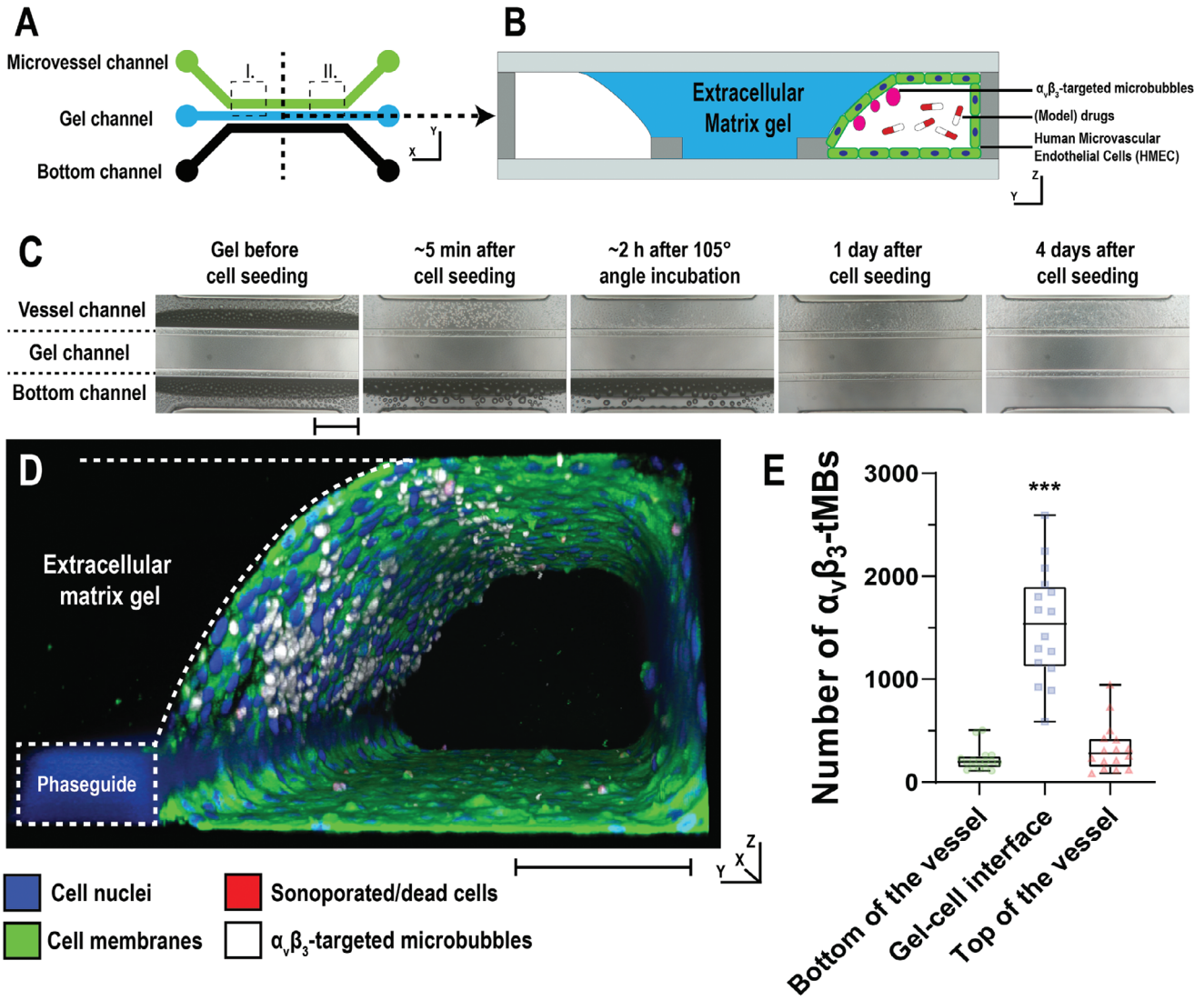

Figure 1. Formation of microvessel-on-chip model and live cell 3D imaging. A) Schematical representation of the three microfluidic channels from the top view with their in- and outlets. Dotted outlines I and II indicate the locations where 3D confocal microscopy images were made. B) Side view of a cross-section of the microvessel-on-a-chip model as used during the experiments (not drawn to scale). The $\alpha_v\beta_3$-targeted microbubbles adhered to the endothelial cell-gel interface and model drugs were added to the lumen of the vessel. C) Brightfield images of the gel seeding and vessel formation over time. The scalebar represents 500 µm. D) 3D confocal microscopy image made at the location I in (A) of a live microvessel-on-chip 4 days after seeding (corresponding confocal microscopy recording animation in Video S1, Supporting Information). The scalebar represents 100 µm for the y-z direction; the x-direction is 635 µm. E) Number of bound $\alpha_v\beta_3$-targeted microbubbles in live microvessels-on-chip (n = 16 fields of view), including the example in D. Boxplot represents the median and the boxes indicate the 25th and 75th percentiles with whiskers ranging from the minimum to maximum value. Significance is indicated with *** ($p < 0.001$). $\alpha_v\beta_3$-tMBs = $\alpha_v\beta_3$-targeted microbubbles.

microphysiological 3D model was cultured which is more representative of the in vivo situation in comparison to glass or membrane substrates used in 2D models.[42]

The expression of the angiogenic biomarker $\alpha_v\beta_3$ by the microvascular cells in the chip was confirmed using immunohistochemistry, albeit non-specific staining in the ECM gel was observed for the secondary antibody in both the $\alpha_v\beta_3$ and isotype control (Figure S2, Supporting Information). The low fluorescence intensity at the phase guide and vertical wall opposite the cell-gel layer is likely an imaging artifact caused by laser refraction from these vertical structures as they are parallel to the laser direction. This explanation is strengthened by the nuclear signal being stronger on the gel layer than on the vertical structures, while the laser intensity per z-plane is the same and there is no biological reason to assume that the nuclear staining would be weaker in some cells than other. Live cell 3D confocal microscopy imaging of a 635 µm wide section of the microvessels was performed following $\alpha_v\beta_3$-tMB incubation under a 75° angle (Figure 1D; Video S1, Supporting Information; $\alpha_v\beta_3$-tMB in white) as this angle resulted in the best binding of the $\alpha_v\beta_3$-tMB to the membrane-fee layer (note this angle is different from the angle used for cell seeding). Quantification of 16 live cell 3D images

in eight different microvessels revealed that a median of $1.5{\cdot}10^3$ (interquartile range: $1.1{\cdot}10^3$–$1.9{\cdot}10^3$) $\alpha_v\beta_3$-tMBs bound to the gel-cell interface layer (Figure 1E). This was a significant 5.5 and 7.7 fold higher in comparison to the bound $\alpha_v\beta_3$-tMBs on the top and bottom of the microvessel respectively. The $\alpha_v\beta_3$-tMB thus predominantly bound to the cellular layer of interest, namely the cells located on the membrane-free gel-cell interface layer which has an extravascular space. This finding indicates that placing the OrganoPlate under a 75° angle during $\alpha_v\beta_3$-tMB administration was effective in selectively targeting the $\alpha_v\beta_3$-tMB by buoyancy to the cells at the gel-cell interface layer. This selective binding of the $\alpha_v\beta_3$-tMB to one side of the microvessel is in line with in vivo observations where $\alpha_v\beta_3$-tMB primarily bound to the top of vessels,[43] likely due to buoyancy. The $\alpha_v\beta_3$-tMB to cell ratio was 3.5:1 (interquartile range: 2.7:1–4.3:1), with the $\alpha_v\beta_3$-tMBs being 80 fold smaller than the mean surface area[44] of an endothelial cell grown under flow. The largest spread in the number of bound $\alpha_v\beta_3$-tMB was found at the gel-cell interface, namely a 4.4 fold difference between the lowest and highest value. Further assessment showed significantly higher $\alpha_v\beta_3$-tMB binding to the left side of the microvessel (location I in Figure 1A) compared to the right side (location II in Figure 1A) (Figure S3, Supporting Information). This difference is likely a result of the flow direction from the left to the right side of the microvessel during $\alpha_v\beta_3$-tMBs addition. Hence, the first opportunity for the $\alpha_v\beta_3$-tMBs to bind is to the cells on the left side of the microvessel. This means that the left side of the microvessel is exposed to all incoming $\alpha_v\beta_3$-tMBs while the right side is only exposed to the $\alpha_v\beta_3$-tMBs that did not yet bind to the microvessel, thereby creating a concentration difference.

2.2. Barrier Integrity Investigation in the Microvessel-on-a-Chip Model

To investigate vascular permeability, the leakage of a 150 kDa fluorescent FITC-dextran model drug over time was studied in a cell-free, non-treated (sham), $\alpha_v\beta_3$-tMB-only, ultrasound only (2 MHz, 750 kPa; 10 × 1000 cycles) and ultrasound (2 MHz, 750 kPa; 10 × 10 or 10 × 1000 cycles) plus $\alpha_v\beta_3$-tMB treated microvessels (typical fluorescent image examples in **Figure 2A**). In the cell-free chips, the FITC-dextran already leaked into the bottom vessel before the first image was made, indicating the absence of a barrier. For the microvessels, the FITC-dextran gradually leaked similarly into the gel and bottom channel in the initial state, i.e., before treatment, as also quantified in Figure 2B. In the initial state, the leakage in these microvessels was below 50%. To ensure similarity in barrier function between the studied microvessels, it is common to exclude microvessels that have an insufficient barrier function[31] due to, for example, differences in gel seeding or cell growth.[32,45] We therefore excluded microvessels when the leakage exceeded 50% within the initial state. This resulted in the exclusion of 34% of all grown microvessels. Of these excluded microvessels, 71% were part of the section of the OrganoPlate in which the BI assay was performed first. Another Organoplate study using transepithelial electrical resistance as readout for permeability suggested that factors like flow and liquid level change can induce permeability changes at the start of the assay which can recover over time.[46] The higher initial leakage observed in the first section of the OrganoPlates in our study is therefore likely caused by moving the plate from the incubator to the experimental setup as this changes the flow and liquid levels. At the same time, the observed increase in leakage in the initial state was far less pronounced in the second section of the OrganoPlate, indicating recovery. For future studies, it may therefore be beneficial to wait with starting the BI assay until some time after the plate has been moved.

For the controls, the leakage in the sham, $\alpha_v\beta_3$-tMB-only, and ultrasound-only conditions was unaffected after the initial state, resulting in a final leakage percentage (median with interquartile range and n-number between brackets) of ≈73% (62%–83%; n = 36) at the end of the BI assay. By contrast, a clear increase in leakage was observed for the ultrasound plus $\alpha_v\beta_3$-tMB conditions after treatment. At the end of the BI assay, the leakage was ≈89% (85%–92%; n = 8) for the 750 kPa 10 × 10 cycles plus $\alpha_v\beta_3$-tMB condition, while this was ≈98% (93%–100%; n = 9) for the 750 kPa 10 × 1000 cycles plus $\alpha_v\beta_3$-tMB condition. Following 0.1% Triton-X addition, the leakage percentage of all microvessels was 100% (100%–100%; n = 122), which indicates that the microvessels having leakage of ≈89% at the end of a BI assay still had a barrier.

2.3. The Effect of Acoustic Pressure and Pulse Length on Vascular Apparent Permeability

The vascular apparent permeability (P_{app}) was calculated before and after treatment from the obtained leakage patterns in the BI assay. Four control (sham; $\alpha_v\beta_3$-tMBs only; 750 kPa 10 × 10 cycles ultrasound only; 750 kPa 10 × 1000 cycles ultrasound only) and ten different ultrasound plus $\alpha_v\beta_3$-tMBs treatment conditions (5 different in situ acoustic pressures ranging from 90–750 kPa at 10 × 10 or 10 × 1000 cycles) were investigated in a total of 122 microvessels, in six different OrganoPlates. In the initial state (i.e., before treatment), only one significant difference in P_{app} was observed, namely between the sham and the 750 kPa 10 × 1000 cycles ultrasound-only condition (Figure S4, all p-values in Table S1, Supporting Information). This significant difference likely occurred due to differences in vessel growth during culture.[45] To address this difference between the control conditions in the initial state, the post-treatment increases in vascular permeability were considered significant when different compared to all four control conditions. After ultrasound plus $\alpha_v\beta_3$-tMB treatment, a significant increase in P_{app} was observed for the highest applied acoustic pressure of 750 kPa at both 10 × 10 cycles and 10 × 1000 cycles and the second highest applied acoustic pressure of 550 kPa at 10 × 1000 cycles in comparison to the control treatments (**Figure 3**; all p-values in Table S2, Supporting Information). Specifically, in comparison to the ultrasound-only control condition of 750 kPa and 10 × 1000 cycles, the P_{app} for the ultrasound plus $\alpha_v\beta_3$-tMBs treated microvessels was ≈2.4 fold higher for 750 kPa and 10 × 10 cycles while this was ≈3.5 fold higher for 550 kPa and 10 × 1000 cycles and ≈5 fold higher for 750 kPa and 10 × 1000 cycles. This finding shows that higher ultrasound pressures increasingly enhanced the vascular permeability upon $\alpha_v\beta_3$-tMB-mediated treatment, which is in line with what others have observed in vivo using chicken embryo[20] and mouse cranial[22] and tumor window[23,47] models for 10,[20]

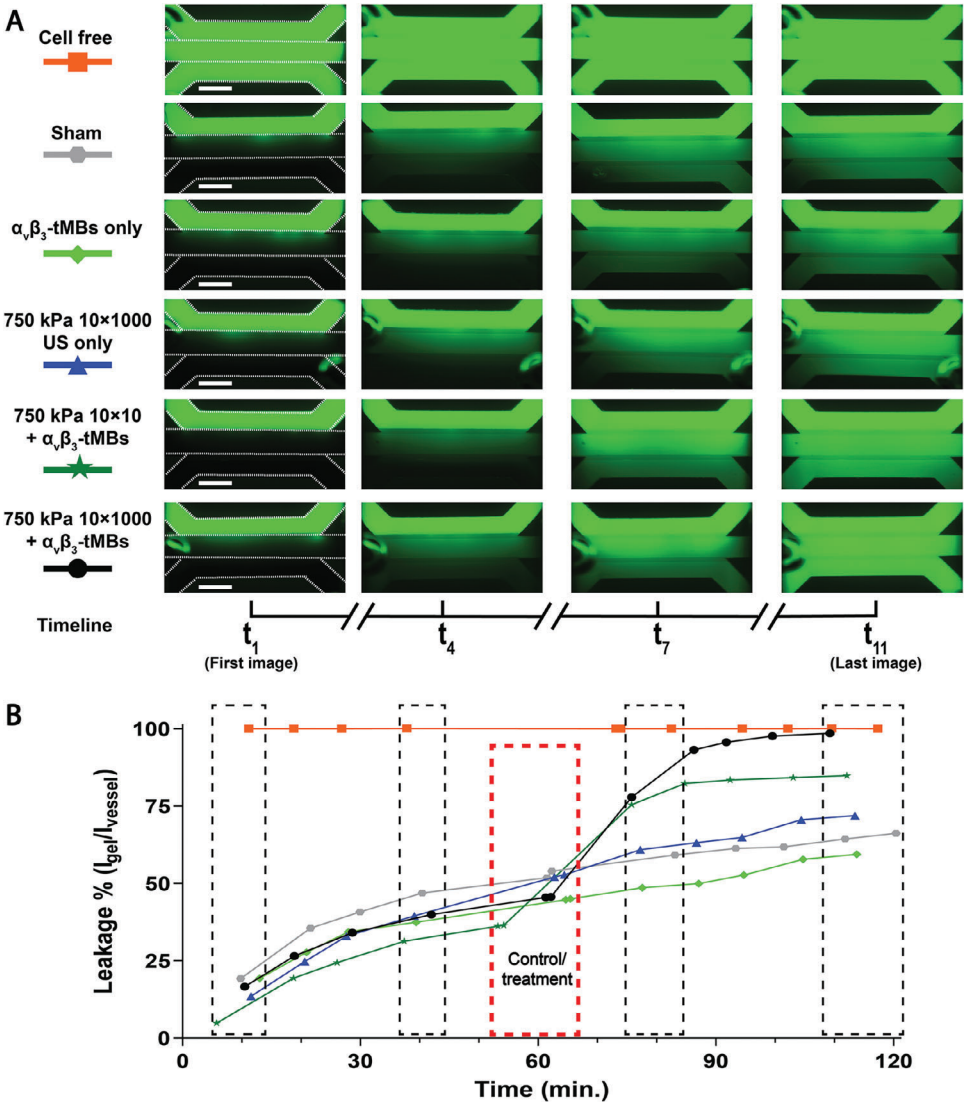

Figure 2. Barrier integrity assay for six different treatment conditions. A) Four selected representative images from the fluorescent microscopy sequence of images visualizing the 150 kDa FITC-dextran model drug leakage over a 2 h period. The three channels in the chip (from top to bottom: microvessel channel, gel channel, bottom channel) are outlined with white-dotted lines in the most left images. Scale bars represent 500 µm. B) Leakage % (i.e., $Intensity_{gel}$/ $Intensity_{vessel}$) over time quantified from the sequence of fluorescent microscopy images. The black-dotted rectangles indicate the time in which the four images shown in A were recorded. The red dotted rectangle indicates the ultrasound treatment (2 MHz; 750 kPa peak negative pressure and 10 × 10 or 10 × 1000 cycles) for the conditions US only and US plus $\alpha_v\beta_3$-targeted microbubbles ($\alpha_v\beta_3$-tMBs).

100,[22] 5000,[47] and 10 000[22] cycle-pulses. While these vascular permeability studies varied the ultrasound pressure and kept the cycle length the same, other vascular permeability studies kept the ultrasound pressure the same and varied the cycle length.[21] At 1 MHz and 850 kPa, Amate et al.,[21] found that the 10, 40, and 5000 cycle pulses all induced antibody extravasation into breast tumors in mice 10 min post-treatment. Their finding that the highest accumulation was induced by the 5000-cycle pulse is in line with our finding that the P_{app} for microvessels treated with $\alpha_v\beta_3$-tMBs at 750 kPa and 10 × 10 cycles was a significantly 2.5 fold lower than at 750 kPa and 10 × 1000 cycles. On the other hand, Morse et al.,[19] found no significant difference in the amount of extravasated dextran in mice brains through the opening of the blood-brain barrier with 5 or 10 000 cycle bursts at 1 MHz and 350 kPa. A plausible explanation for the difference is the different location of the vessels: either outside of the brain or within the brain. A previous vessel-on-a-chip study showed significantly more cell–cell junction opening was induced with ultrasound pulses with a mechanical index (MI; defined as $P / \sqrt{f}$, where P is the peak negative pressure of the ultrasound wave (in MPa) and f is the center frequency of the ultrasound wave (in MHz)[48] of 0.72 compared to an MI of 0.4 (600 × 500 cycles), which could explain why leakage in our model was only observed with the higher ultrasound pressures.[30] In addition, our findings that bursts of just 10 cycles can already increase vascular permeability are in agreement with a previous in vivo chicken embryo study.[20] The minimum pressure to induce permeability in our study using 2 MHz ultrasound was 750 kPa for 10 × 10 cycles

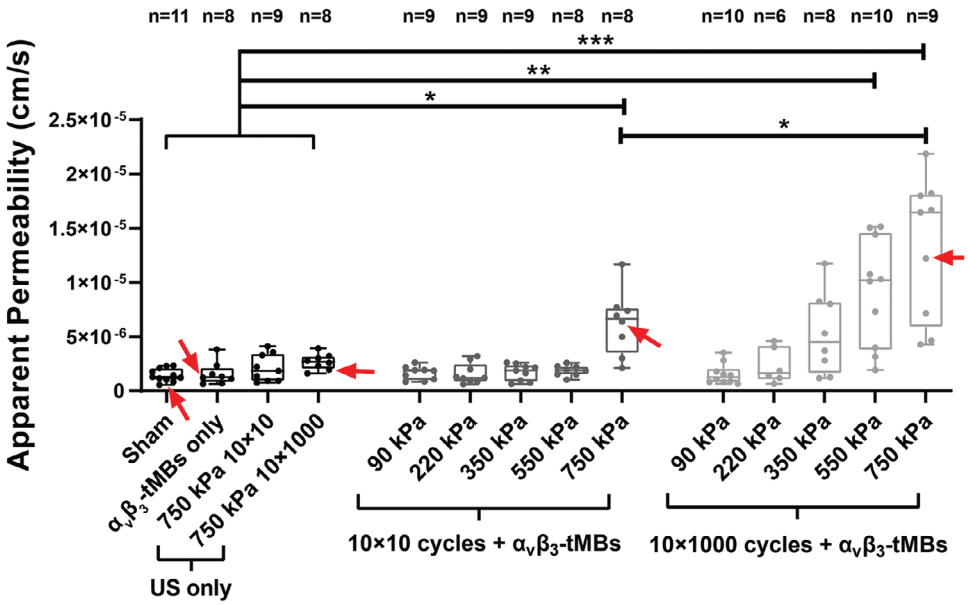

Figure 3. Apparent permeability after treatment for four control (on left) and ten treatment conditions. Boxplot represents the median with the boxes indicating the 25th and 75th percentiles with whiskers ranging from the minimum to maximum value. Significance between the four control and ten treatment conditions is indicated with $^{*}p < 0.05$, $^{**}p < 0.01$, and $^{***}p < 0.001$. See Table S2 (Supporting Information) for all statistical comparisons. Datapoints that correspond to the example vessels shown in Figure 2 are indicated with red arrows. US = ultrasound; $\alpha_v\beta_3$-tMBs = $\alpha_v\beta_3$-targeted microbubbles.

(i.e., MI = 0.53) plus $\alpha_v\beta_3$-tMBs and 550 kPa for 10 × 1000 cycles (i.e., MI = 0.39) plus $\alpha_v\beta_3$-tMBs. These MI values are in agreement with the minimum MI to induce permeability in mouse cranial window[22,49] (i.e., MI = 0.37 with 600 × 100 cycles and MI = 0.55 with 120 × 12 000 cycles) studies and a tumor window[23] study (i.e., MI = 0.4 with 150 × 1000 cycles). On the other hand, the MI of 0.53 needed to induce permeability for the shorter 10 × 10 cycle treatment plus $\alpha_v\beta_3$-tMBs in our study was considerably lower than the previously reported needed MI of 1.3 for the 2500 × 10 cycle plus MB treatment in a chicken embryo study.[20] A plausible explanation for this difference is the smaller vessels with diameters of 12–21 µm that were studied in the chicken embryo in comparison to 200–300 µm vessels in the OrganoPlate 3-lane, as other studies have reported that the MB's oscillation amplitude is 2–3 fold less in 25 than 160–200 µm diameter capillary tubes[50,51] due to the closer proximity of the opposite wall to the MBs.[50]

2.4. Onset Rate and Spatial Distribution of the Vascular Permeability

For the three ultrasound plus $\alpha_v\beta_3$-tMB treatment conditions that showed a significant increase in P_{app} in comparison to the four control conditions (see Figure 3), the onset rate of the leakage was further investigated during the first 5 min after treatment using time-lapse imaging as presented in **Figure 4**. For the sham and 750 kPa 10 × 1000 cycles ultrasound-only control treatments, no increases in leakage were observed in the microvessels during the first 5 min after treatment (Figure 4A and zoom-in in Figure 4B), which is in line with the findings presented in Figure 2. We hardly observed any increase in leakage during the first 5 min after treatment for the 750 kPa 10 × 10 cycles plus $\alpha_v\beta_3$-tMB treatment, while the mean leakage percentage did reach 71% at the end of the BI assay (Figure 4A and zoom-in in Figure 4B). By contrast, for the 550 and 750 kPa 10 × 1000 cycles ultrasound plus $\alpha_v\beta_3$-tMBs treatment conditions, a clear increase in leakage was observed during the first 5 min after treatment (Figure 4A and zoom-in in Figure 4B). At the end of the BI assay, the mean leakage percentage reached 96% for the 550 kPa and 97% for the 750 kPa 10 × 1000 cycles plus $\alpha_v\beta_3$-tMB treated vessels. The increase within the first 5 min upon treatment was lower and the onset rate was 3 fold slower for the 550 kPa than the 750 kPa plus $\alpha_v\beta_3$-tMB condition. This is in line with previous in vivo studies that reported significantly faster extravasation rates for higher acoustic pressures in a chicken embryo model (700 vs 1300 kPa; 10 cycles at 1 MHz)[20] and faster extravasation onset times for higher acoustic pressures in a mouse tumor window model (200 vs 800 kPa; 10 000 cycles at 1 MHz).[23] In our study, the calculated P_{app} showed no significant differences between the treatment conditions in the initial state, while the P_{app} during the first 5 min after treatment (Figure 4C) showed a similar trend as the P_{app} for 1.5 h after treatment (Figure 3), although not significant.

The 5 min time-lapse recordings showed that the vascular permeability increase started in a spot-wise pattern for all the ultrasound plus $\alpha_v\beta_3$-tMB conditions (Figure 4D; Video S2, Supporting Information), including the 750 kPa 10 × 10 cycle plus $\alpha_v\beta_3$-tMB condition that hardly had an increase in leakage percentage and P_{app}. The spot-wise pattern is in line with previous chicken embryo[20] and mouse model[23] studies where the ultrasound plus MB-induced leakage also originated from single spots. In our study, we observed that the initial leakage spots were unevenly distributed over the microvessel and

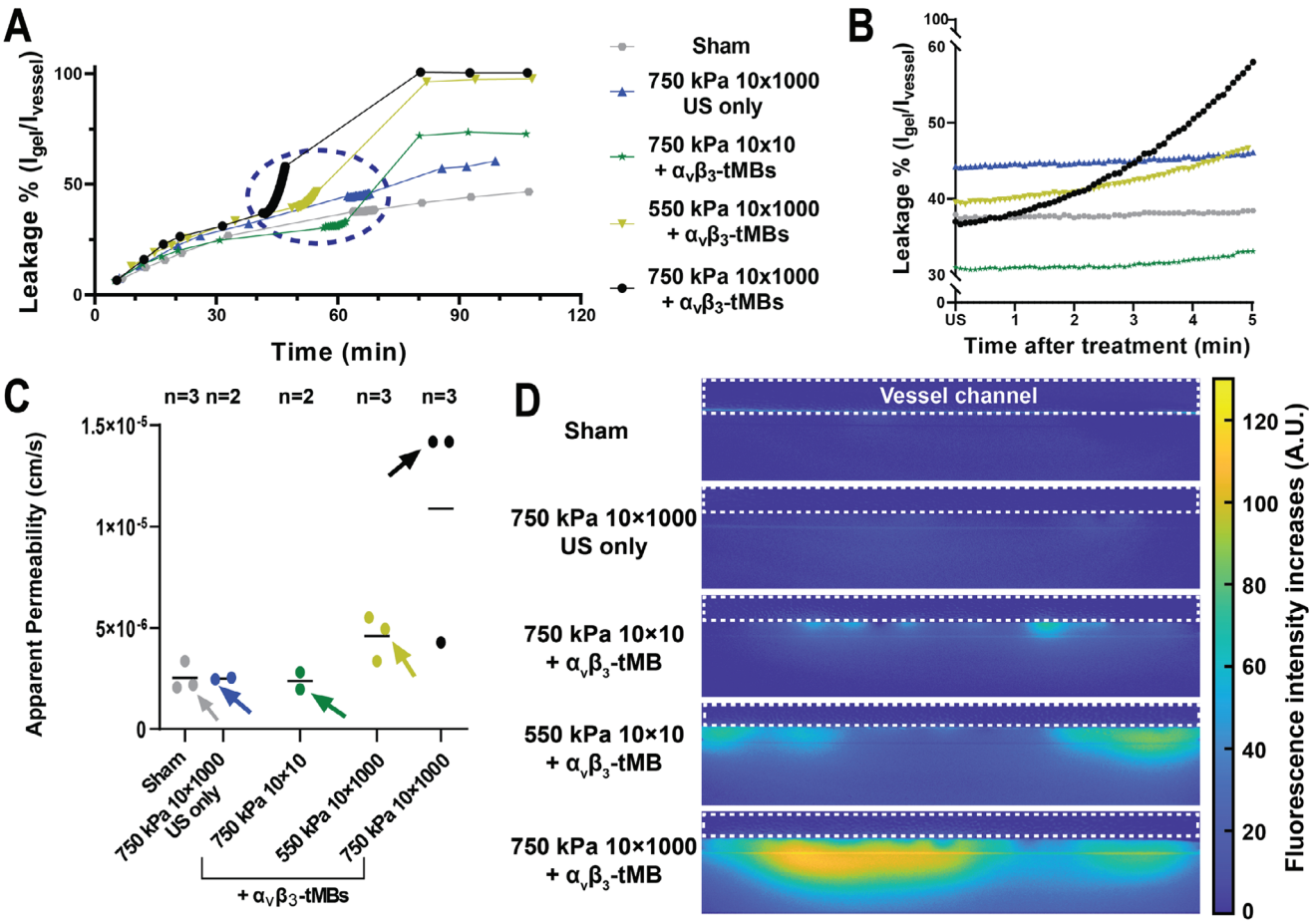

Figure 4. The onset rate and spatial distribution of the vascular permeability increase. A) Leakage % (Intensity$_{gel}$/ Intensity$_{vessel}$) over time with the integrated 5 min time-lapse imaging in the blue-dotted circle. B) Zoom-in of the blue-dotted circle of Figure 4A showing the leakage % during the 5 min time-lapse imaging directly after treatment. C) Apparent permeability (P_{app}) during the first 5 min after treatment. Datapoints represent individual vessels, with arrows indicating the data points corresponding to the examples shown in Figure 4A,B,D, and lines indicate the mean per condition. No statistically significant differences were observed. D) Visualization of the spatial distribution of the leakage 5 min after treatment. US = ultrasound; $\alpha_v\beta_3$-tMBs = $\alpha_v\beta_3$-targeted microbubbles; A.U. = arbitrary unit.

varied in number per microvessel, which could be a result of the previously observed differences in microbubble concentrations in Figure 1E.

2.5. The Effect of the Microbubble-Mediated Treatment on Sonoporation

Before treatment with 750 kPa 10 × 1000 cycle ultrasound plus $\alpha_v\beta_3$-tMBs, hardly any propidium iodide (PI) was observed in the 3D confocal microscopy image of part of the microvessel (**Figure** 5A), suggesting the number of dead cells was negligible. One and a half hour after treatment, an increase in PI signal was mainly observed in the cells located at the gel-cell interface layer (Figure 5A). As PI stains dead[52] and alive sonoporated[9] cells by entering the cells and becoming fluorescent upon intercalation with RNA and DNA,[53] the distinguishment between dead or sonoporated cells cannot be made 1.5 h after treatment. However, this difference can be made up to 120 s after treatment as membrane pores remaining open for more than 120 s do not close,[9,35,54] consequently resulting in cell death.[35] In the initial state, the only significant difference in PI signal was between the sham and lower 550 kPa 10 × 1000 cycles plus $\alpha_v\beta_3$-tMBs treatment (Figure S5, all p-values in Table S3, Supporting Information). Figure 5B shows the change in PI signal within 45 s after treatment. As for the P_{app}, post-treatment increases were considered significant when different compared to all four control conditions. For the 10 × 10 cycles plus $\alpha_v\beta_3$-tMB conditions, the change in PI signal was only significantly higher for the 750 kPa pressure (2.9% increase) (all p-values in Table S4, Supporting Information). For the 10 × 1000 cycles plus $\alpha_v\beta_3$-tMB conditions, a significant change in PI signal was observed for the four highest pressures: 2.5% increase at 220 kPa, 7.3% increase at 350 kPa, 24.5% increase at 550 kPa and 28.5% increase at 750 kPa. In addition, the 550 and 750 kPa 10 × 1000 cycles plus $\alpha_v\beta_3$-tMB conditions also showed a significantly higher change in PI in comparison to all other ultrasound plus $\alpha_v\beta_3$-tMB treatment conditions. Our findings are in line with two other in vitro studies,[35,55] which showed that the higher the acoustic pressure was, the more cells were sonoporated. These

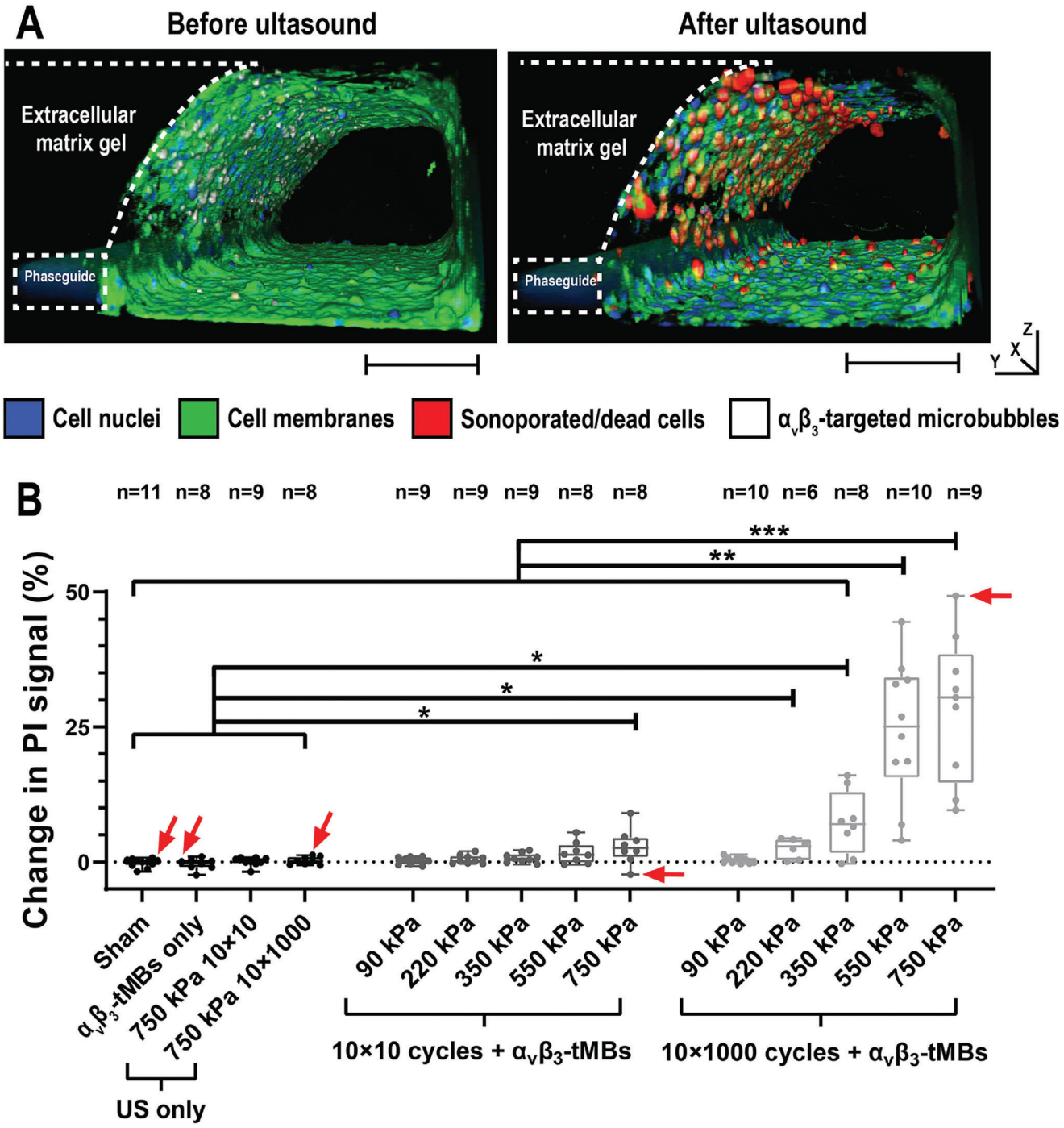

Figure 5. Sonoporation of cells in microvessel-on-chip after treatment. A) 3D confocal microscopy image of part of a microvessel before (left) and 1.5 h after 750 kPa 10 × 1000 cycles of ultrasound plus $\alpha_v\beta_3$-tMBs treatment (right). The scalebar represents 100 µm for the y-z direction; the x-direction is 635 µm. B) Percentage change in PI signal within 45 s after treatment. The boxplot represents the median and the boxes indicate the 25th and 75th percentiles with whiskers ranging from the minimum to maximum value. Statistical significance is indicated with $^{*}p < 0.05$, $^{**}p < 0.01$, $^{***}p < 0.001$. See Table S4 (Supporting Information) for all statistical comparisons. Datapoints that correspond to the example vessels shown in Figure 2 are indicated with red arrows. PI = propidium iodide; US = ultrasound; $\alpha_v\beta_3$-tMBs = $\alpha_v\beta_3$-targeted microbubbles.

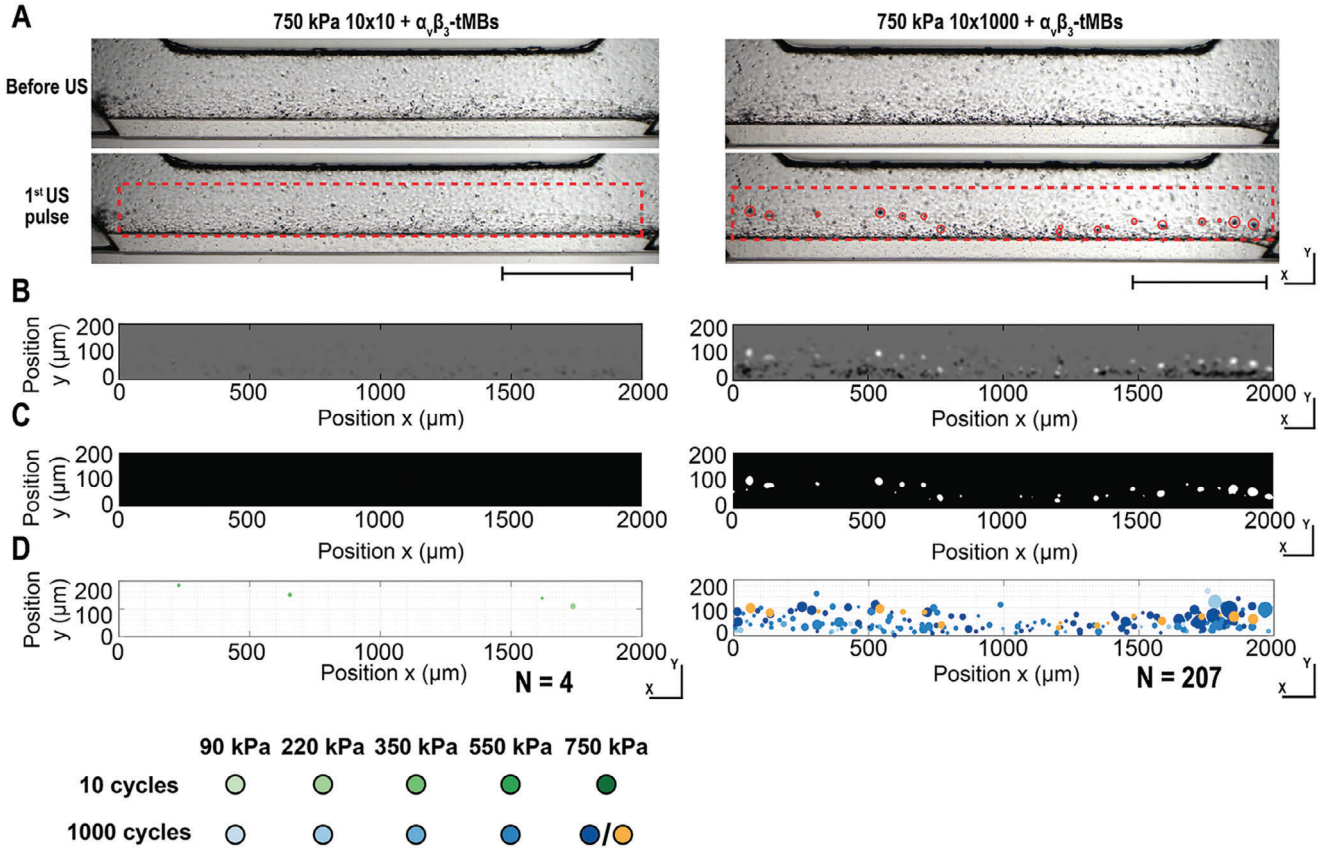

Figure 6. $\alpha_v\beta_3$-Targeted microbubble cluster formation during ultrasound treatment. A) Example images of the microvessels from Figure 4 before ultrasound (US) (top row) and after the first US pulse (bottom row). Red-dotted rectangles indicate the ROI for the cluster analysis and red circles highlight the formed $\alpha_v\beta_3$-tMB clusters. The scalebar represents 500 μm. B) Difference in signal after the first ultrasound pulse with black indicating signal increase (i.e., more light goes through) as a result of tMB displacement and white indicating signal decrease (i.e., less light gets through) as a result of tMB cluster formation. C) Mask based on the signal decrease from Figure 6B. D) Schematic representation of all tMB cluster locations and sizes obtained from 48 (left) and 46 (right) microvessels. Circle locations, sizes, and colors correspond with the cluster locations, cluster sizes, and treatment conditions. The orange points in the 1000 cycles graph correspond with the tMB clusters in Figure 6A. (A–D) Microvessels treated with 750 kPa plus $\alpha_v\beta_3$-tMB at 10 × 10 cycles (left) and 10 × 1000 cycles (right).

studies used 1 MHz ultrasound with pressures ranging from 100–500 kPa at 2000 cycles[55] or 140–500 kPa at 500–50 000 cycles.[35] The latter study also reported an increase in sonoporation for longer cycle treatments,[35] which is also in line with our findings.

2.6. The Effect of the Ultrasound Pulse Length on Microbubble Behavior

The optical bright field recordings showed that the bound $\alpha_v\beta_3$-tMB displaced during the 10 ultrasound pulses. For the 750 kPa 10 × 10 cycle condition, shown in the left panels of **Figure 6**A–C and Video S3 (Supporting Information), $\alpha_v\beta_3$-tMBs displaced at the far right of the vessel channel near the gel-cell interface layer, while displacement occurred throughout the vessel channel for the 750 kPa 10 × 1000 cycle condition (right panels of Figure 6A–C; Video S4, Supporting Information). The displacement of tMBs bound to a surface by the application of ultrasound has been observed before,[35,56,57] and is caused by secondary Bjerknes forces, i.e., the mutual interaction between oscillating MBs. Following the displacement of the $\alpha_v\beta_3$-tMBs, the formation of MB clusters was observed. In the 10 × 10 cycles condition, a total of four clusters formed divided over the 46 microvessels, whereas a total of 207 clusters formed divided over the 48 microvessels in the 10 × 1000 cycles condition (Figure 6D; Table S5, Supporting Information), where the orange dots indicate the clusters from Figure 6A. This difference suggests that cluster formation predominantly occurred after longer cycle insonification, which is in line with what others have observed.[56–58] In the OrganoPlate 3-lane, cluster formation occurred more often at the left and right side of the microvessel close to the ends of the PhaseGuides (Figure 6D). However, no pattern in the distance between clusters was found (Figure S6, Supporting Information), thereby indicating that standing waves[59] were not the main mechanism leading to tMB clustering. Instead, it is more plausible that the tMB clusters were induced by secondary Bjerknes forces as these forces have previously been shown to induce MB clusters upon ultrasound insonification in a 200 μm capillary.[60] In addition, others have reported that the number of formed MB clusters increased upon longer ultrasound insonification time.[61]

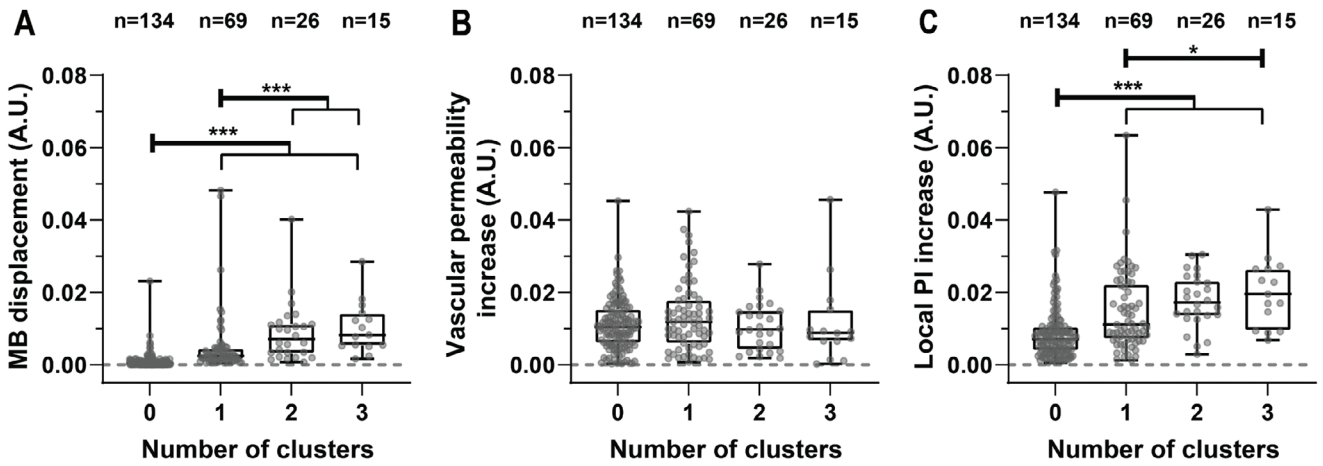

Figure 7. Local relations with the number of formed $\alpha_v\beta_3$-tMB clusters per 200 µm segments in the microvessels after the first cycle of ultrasound. A) Local relation between formed $\alpha_v\beta_3$-tMB clusters and $\alpha_v\beta_3$-tMB displacement. B) Local relation between formed $\alpha_v\beta_3$-tMB clusters and vascular permeability increase. C) Local relation between formed $\alpha_v\beta_3$-tMB clusters and propidium iodide (PI) increase (i.e., sonoporation). (A–C) Boxplots represent the median and the boxes indicate the 25th to 75th percentiles with whiskers ranging from the minimum to maximum values. Every data point and n-number represents individual microvessel segments of 200 µm. Statistical significance is indicated with $^{*}p < 0.05$ and $^{***}p < 0.001$. MB = $\alpha_v\beta_3$-targeted microbubble; A.U. = arbitrary unit; PI = propidium iodide.

2.7. Relation Between Vascular Permeability, Sonoporation, and $\alpha_v\beta_3$-tMB Clustering

The relation between $\alpha_v\beta_3$-tMB cluster formation and $\alpha_v\beta_3$-tMB displacement, vascular permeability increase (i.e., leakage increase), and sonoporation (i.e., PI increase), was evaluated by segmenting the treated microvessels in 200 µm segments. Only the 550 and 750 kPa 10 × 1000 cycles plus $\alpha_v\beta_3$-tMB conditions were selected for the analysis because these conditions showed a significant increase in P_{app} (Figure 3) and contained 86% of all formed $\alpha_v\beta_3$-tMB clusters (Table S5, Supporting Information). Segments with higher $\alpha_v\beta_3$-tMB displacement after the first ultrasound pulse showed significantly more cluster formation (**Figure** 7A). As shown in Figure 7B, no relation was found between the number of $\alpha_v\beta_3$-tMB clusters and vascular permeability increase. This finding is in line with others who reported that MB behavior could not predict cell-cell contact opening.[9] By contrast, more $\alpha_v\beta_3$-tMB cluster formation resulted in significantly more sonoporation within the same vessel segment after the first ultrasound pulse (Figure 7C). Other in vivo work also showed that MB clusters sonoporated more cells than single MBs and the sonoporation rate increased with bigger MB clusters,[62] thereby validating the robustness of our model. For the applied consecutive ultrasound pulses, the number of $\alpha_v\beta_3$-tMB clusters decreased suggesting the clusters moved, merged, and/or dissolved (Figure S6, Supporting Information). The consecutive pulses showed less significant relations between $\alpha_v\beta_3$-tMB clusters, $\alpha_v\beta_3$-tMB displacement, and sonoporation (Figure S7, Supporting Information). A possible explanation for the observed differences between the first and later applied cycles of ultrasound is that the merging of the clusters will change the cavitation mechanism. We expect much more stable cavitation since clusters are known to have a (much) lower resonance frequency than single microbubbles.[61] At the used 2 MHz insonification frequency, i.e., (far) above the resonance frequency of the merged cluster, the relative cluster vibration amplitude will be small compared to the relative vibration amplitude of single microbubbles[58] because these single microbubbles are excited on or around their resonance frequency. To verify this possible explanation, ultra-high-speed imaging can be used as this technique has been shown to determine oscillation amplitudes of both single MBs[8,9] and MB clusters.[63] A limitation of our study is that ultra-high-speed imaging was not feasible to visualize the MB oscillations due to technical challenges as a combination of an objective with a long working distance, high resolution, and high magnification is needed. Instead, passive cavitation detection[64] could be used to gain insight into the response of the MB population within the microvessel-on-a-chip model.

Further investigation into the relation between vascular permeability increases and sonoporation per microvessel segment (**Figure** 8) showed no significant correlation above the control threshold (Figure S8, Supporting Information) for any of the treatment conditions. The absence of this correlation is underlined by the 220 and 350 kPa 10 × 1000 cycles plus $\alpha_v\beta_3$-tMB treatments, which both resulted in no significant vascular permeability increase (Figure 3) while sonoporation was significantly increased (Figure 5B). It is unlikely that diffusion of the FITC-dextran contributed to the lack of correlation because the leakage spots were identified in the first frame after ultrasound treatment, i.e., the first frame of Video S2 (Supporting Information), meaning that diffusion was still very minimal in comparison to the full 5 min video. A plausible explanation for the lack of correlation is that we were only able to detect PI signals from nuclei and not the cytoplasm because the PI signal is higher upon binding to DNA in the nucleus in comparison to the lower signal when binding to RNA in the cytoplasm. The finding that PI uptake can be low and limited to the cytoplasm for tunnel formation and cell–cell contact opening from our previous 2D studies,[9,11] supports this explanation. Our findings in the OrganoPlate do suggest that an increase in vascular permeability is only induced in microvessels in which sonoporation also occurred, while sonoporation can also be induced in the absence

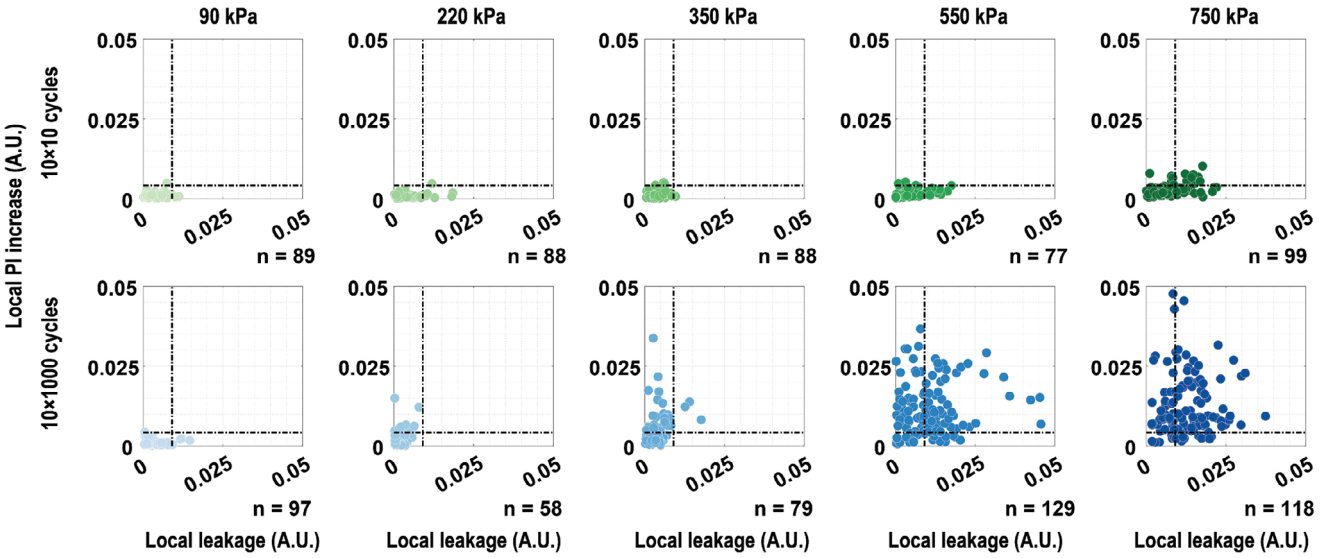

Figure 8. Correlation between vascular permeability increase (i.e., leakage) and sonoporation (i.e., propidium iodide uptake) in the microvessels for the ultrasound plus $\alpha_v\beta_3$-tMB treatments. The top row is the 10 × 10 cycle treatment and bottom row the 10 × 1000 cycle treatment with colors corresponding to the treatment conditions as illustrated in Figure 6D. Every data point and n-number represent individual microvessel segments of 200 µm. The dotted lines indicate the thresholds obtained from the control conditions as presented in Figure S8 (Supporting Information). No statistically significant correlations were observed. PI = propidium iodide; A.U. = arbitrary unit.

of an increase in vascular permeability. An increase in vascular permeability can be a result of trans-endothelial tunnel formation upon sonoporation,[11,17] which creates transcellular gaps,[65] and/or cell–cell junction opening,[8,11,66] which creates paracellular gaps. The physiological implications are that tunnel formation likely induces a shorter increase in vascular permeability than cell–cell junction opening because tunnels are known to close within 20 min[67] and it may take longer for cell–cell junctions to restore. It remains unclear whether microbubble-induced vascular permeability in our microvessel-on-a-chip model is caused by tunnel formation or cell junction opening because it is technically challenging to optically visualize these mechanisms in a 3D structure of this size. We now studied the vascular permeability up to 72 min post-treatment, which could be extended in future studies to investigate for how long the vascular permeability remains increased. By adding the dextran at different time points after treatment, the restoration of the vascular permeability can be studied. Amate et al.,[21] discovered that the 40 cycle pulse was more favorable than the 10 and 5000 cycle pulse for antibody accumulation in tumors based on the number of vessels in which extravasation was induced, how much antibody accumulated, and the range to which the antibodies extravasated from the vessel at both the 10 min and 4 h time point. Interestingly, the 5000 cycle pulse resulted in the antibody getting extravasated the furthest from the vessels but 4 h after treatment the accumulation had faded. In the brain, a 5 cycle pulse was shown to only open the blood-brain barrier for less than 10 min while the dextran was delivered more uniformly throughout the parenchyma with 3.4 fold less release of albumin.[19] Taken together, these studies illustrate that the applied ultrasound parameters have physiological implications, which would benefit from further investigations.

In our study, we used cell medium as fluid in the lumen of the microvessel. For future studies, whole blood could be used instead of cell culture medium to investigate the attribution of for example red blood cells to drug delivery as red blood cells have been shown to contribute to the microbubble-mediated induced bioeffects in vivo.[68] At the same time, the effect of the increase in viscosity for whole blood in comparison to cell culture medium needs to be investigated with regards to MB behavior, including MB clustering, vascular permeability increases, and sonoporation. Using non-tMB for studies in the OrganoPlate will be challenging as non-tMB will float up due to buoyancy. As a consequence, non-tMB will not be in contact with the cells grown on the membrane-free gel layer, unless the plate is placed at an angle during the experiments so that the gel layer is orientated to the top.

2.8. The Effect of the Microbubble-Mediated Treatment on Microvessel Viability

The effect of the ultrasound plus $\alpha_v\beta_3$-tMB treatment on the cell viability 78 min after treatment was investigated in 60 cell-containing microvessels divided over nine different treatment conditions and one positive and four negative controls using a WST-8 colorimetric assay, as presented in **Figure 9**. The positive and negative controls had a significantly lower mean absorbance value of ≈0.3 in comparison to 0.8–0.9 for all treated cell-containing microvessels (all p-values in Table S6, Supporting Information). No significant differences in viability on a microvessel level were observed between all the sham, $\alpha_v\beta_3$-tMB only, ultrasound only, and ultrasound plus $\alpha_v\beta_3$-tMB treatments. Yet, ≈4% cell death has previously been reported for endothelial cells treated with ultrasound (1 MHz, 500 kPa (MI 0.5), 1 × 1000 cycles) plus CD31-tMB.[35] The reason for the difference in cell viability between their 2D in vitro and our 3D in vitro study could

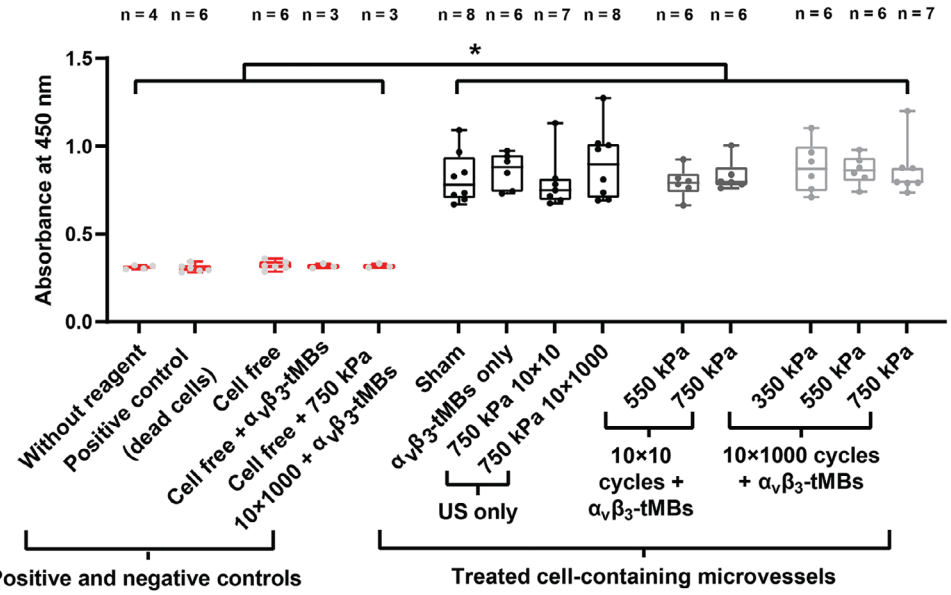

Figure 9. Microvessel viability after treatment was measured with a WST-8 colorimetric assay. Boxplots represent the median and the boxes indicate the 25th and 75th interquartile range with whiskers ranging from the minimum to maximum value. A higher absorbance indicates more living cells within the microvessel. Statistical significance is indicated with $^{*}p < 0.05$. See Table S6 (Supporting Information) for all statistical comparisons. US = ultrasound; $\alpha_v\beta_3$-tMBs = $\alpha_v\beta_3$-targeted microbubbles.

be due to differences in the stiffness of the substrate on which the cells were grown, namely a polymer membrane in their study and soft collagen (Young's modulus 0.43–0.68 kPa) in our study. This explanation is supported by a previous study that reported less ultrasound plus MB-induced cell death for cells cultured on a soft substrate (Young's modulus 0.2 kPa) in comparison to a rigid substrate (Young's modulus 40 kPa).[69] At the same time, the death of a few single cells as a result of our treatment cannot be ruled out because a few dead cells are not expected to affect the WST-8 assay results. A few dead cells can also not be the source of the vascular permeabilization spots because apoptosis takes at least 10 min[70] while the leakage spots occur within seconds after treatment (Figure 4B; Video S2, Supporting Information). Besides, if the source of the leakage spots had been dead cells, then a correlation would have been found between the increase in PI signal and leakage as dead cells contain a high PI amount, which was not the case (Figure 8). It is far more likely that the source of the leakage spots was tunnel formation and/or cell–cell contact opening and not cell death because these pathways create gaps through the endothelial layer within 15 s of the treatment.[8,9,11] This timeframe aligns with the observation of the leakage spots. Alternatively, cell detachment could be a source for the leakage spots as ultrasound and microbubble-induced cell detachment has been reported,[71] albeit for much higher acoustic pressures of ≈4 MPa. We therefore quantified the number of nuclei at the gel interface before and after 750 kPa 10 × 1000 and $\alpha_v\beta_3$-tMBs treatment in the acquired confocal z-stacks of the live cells. As shown in Figure S9 (Supporting Information), no significant changes in the amount of nuclei were found, suggesting cell detachment was not a source for the leakage spots.

3. Conclusion

Investigating $\alpha_v\beta_3$-tMB-mediated changes in vascular permeability and sonoporation in a newly developed microvessel-on-a-chip model with a membrane-free extravascular space revealed distinct differences between ultrasound treatments with 10 × 10 and 10 × 1000 cycles. Although both the 10 × 10 cycles and 10 × 1000 cycles of 2 MHz ultrasound induced vascular permeability increases in spot-wise patterns and sonoporation without affecting microvessel viability, the 10 × 10 cycles induced significantly less vascular permeability increase and sonoporation in comparison to the 10 × 1000 cycles at the highest studied PNP of 750 kPa. In addition, the PNP threshold for inducing a vascular permeability increase and sonoporation was higher for 10 × 10 than for 10 × 1000 cycles, making a treatment with longer cycles of ultrasound plus $\alpha_v\beta_3$-tMBs more potent for future therapeutic applications. At the same time, if $\alpha_v\beta_3$-tMB-mediated drug delivery to endothelial cells via sonoporation is only needed, then lower pressures should be used as 220 and 350 kPa at 10 × 1000 cycles induced significant sonoporation in the absence of a vascular permeability increase. Evaluating the microbubble behavior revealed no relation with vascular permeability increases while a relation was found between formed $\alpha_v\beta_3$-tMB clusters and sonoporation. This developed microvessel-on-a-chip model and the novel insights generated with it demonstrate the effect of the ultrasound pressure and cycle length on the vascular permeability increase and sonoporation outcome, which has physiological implications for the type of drug that needs to be delivered intracellularly or beyond the vessel wall. The model therefore aids toward the safe and efficient implementation of MB-mediated local drug delivery.

4. Experimental Section

Cell Culture: Immortalized human dermal microvascular endothelial cells (HMEC-1, CRL-3242, ATCC, Manassas, VA USA) were cultured in MCDB131 medium (10372019, Gibco, Thermo Fisher Scientific, Waltham, MA, USA). This basal medium was supplemented with 10% heat-inactivated fetal bovine serum (FBS, 16122563, Gibco), 10 mM L-Glutamine (G7513, Sigma–Aldrich, Zwijndrecht, the Netherlands), 1 µg mL^{-1} Hydrocortisone (H0135, Sigma–Aldrich), 1% Penicillin-Streptomycin (15140122, Gibco), and 10 ng mL^{-1} Epidermal Growth Factor (EGF) (E9644, Sigma–Aldrich). After thawing, HMEC-1 cells were cultured in T75 flasks for 3 days in a humidified incubator at 37 °C and 5% CO_2.

Microvessel-on-a-Chip: The microvessel-on-a-chip model was created in the OrganoPlate 3-lane 40 (4003-400-B, Mimetas B.V., Leiden, the Netherlands), a microfluidic titerplate with a 384-wells microtiter plate footprint and a bottom consisting of 40 microfluidic chips.[72] As illustrated in Figure 1A,B, each glass-bottomed chip consisted of three parallel microfluidic channels, separated by PhaseGuides.[73] The wells of the titerplate consisted of standard virgin polystyrene and the chip bottom had a standard 1H coverslip thickness (150 µm). The top and bottom channels had a height of 220 µm and a width of 300 µm. The middle channel had a height of 220 µm and a width of 350 µm. Each channel had its own in- and outlet in separate wells which functioned as medium reservoirs and allowed access to both sides of the channels.

To form the hollow tubular-shaped matrix in which the microvessel-on-a-chip was grown, a collagen I extracellular matrix gel was loaded in the middle inlet channel of each chip 1 day before cell seeding. The gel was prepared by mixing 5 mg mL^{-1} Cultrex Rat Collagen I matrix gel (3447-020-01, R&D systems, Bio-Techne, Minneapolis, MN, USA), 1 M HEPES (15630-056, Gibco), and 37 g L^{-1} $HaHCO_3$ pH 9.5 (S5761, Sigma–Aldrich) in an 8:1:1 ratio to a final gel concentration of 4 mg mL^{-1}. The gel mixture was kept cold in an NEB cooler (T0225S, New Engeland BioLabs, Ipswich, MA, USA) during mixing and pipetting. Within 15 min after mixing, 2 µL of the gel was loaded into the OrganoPlate. After loading, the gel was polymerized by incubating the OrganoPlate for 15 min in a humidified incubator at 37 °C and 5% CO_2. After incubation, 20 µL Dulbecco's Phosphate-Buffered Saline (D-PBS) (14190094, Gibco) was added to all the middle channel inlets, and the OrganoPlate was placed in a humidified incubator at 37 °C and 5% CO_2 overnight. Due to the PhaseGuides, the gel stayed contained in the middle channel and formed a meniscus toward the top and bottom channels.[73]

One day after gel loading, the D-PBS was removed from all the middle channel inlets, and 50 µL of 28.5 µg mL^{-1} fibronectin solution (10 838 039 001; Roche Diagnostics Corp., Indianapolis, IN) in non-supplemented MCDB131 medium was added to all the top channel outlets. Next, the OrganoPlate was incubated for 30 min in a humidified incubator at 37 °C and 5% CO_2. The HMEC-1 cells (passage number 24 or 26) were detached with trypsin/EDTA (CC-5012, Lonza), centrifuged at 220 *g*, 5 min, break 2 (Heraeus Biofuge, Thermo Scientific, Etten Leur, the Netherlands), and the cell pellet was resuspended into supplemented MCDB131 medium to reach a concentration of $1.0 \cdot 10^7$ cells mL^{-1}. Subsequently, the cell suspension was seeded into the channel by passive pumping, i.e., adding a 2 µL droplet to the top channel inlet which will flow into the channel until surface tension between the in and outlet is equilibrated.[41] For the cell-free controls, 2 µL of supplemented MCDB131 medium was added to the top channel outlet instead. After cell seeding, fibronectin solution was aspirated from the top channel outlet, and 50 µL of supplemented MCDB131 medium was added. To allow the cells to attach to the gel meniscus, the OrganoPlate was incubated under an angle of 105° on the MIMETAS plate stand in a humidified incubator at 37 °C and 5% CO_2 for 2 h. After incubation, the plate was removed from the stand and 50 µL of supplemented MCDB131 medium was added to the top channel outlet. Next, the OrganoPlate was cultured under flow for 4 days by incubating the plate on the Mimetas OrganoFlow rocker (8 min intervals at 7° inclination angle), exposing the cells to a mean flow rate of 2.02 µL min^{-1} and mean shear of 0.13 dyne cm^{-2},[74] in a humidified incubator at 37 °C and 5% CO_2. Medium from the top channel in- and outlets was refreshed 1 day after cell seeding. Experiments were performed 4 days after cell seeding. Before the experiment started, all middle and bottom channel in- and outlets of each microvessel were wetted by adding 50 µL of supplemented MCDB131 medium to them, after which the plate was incubated for 5 min under a 7° inclination angle in a humidified incubator at 37 °C and 5% CO_2.

Gel Stiffness Measurements: The extracellular collagen I matrix gel was prepared as described above for three different gel Lot Numbers. Five gel drops of 10 µL were seeded in a 35 mm petridish. D-PBS was added in the same gel:D-PBS ratio of 1:10 as used in the OrganoPlate and the gel was incubated overnight in a humidified incubator at 37 °C and 5% CO_2. Before measurements, the samples were fully submerged in D-PBS and the Young's modulus of the gel was measured in nine different locations spaced 10 µm apart in a 3 × 3 grid using a Chiaro Nanoindenter (Optics11life, Amsterdam, the Netherlands) with a 3 µm tip radius probe (Optics11life) as previously reported.[75]

Immunohistochemistry: Four days after cell seeding, immunohistochemistry was performed to visualize the $\alpha_v\beta_3$ integrin expression on the HMEC-1 cells. All incubation steps were performed at room temperature and 100 µL was added to the top channel inlet and 50 µL was added to all the other channels in- and outlets, unless mentioned otherwise. First, the OrganoPlate was incubated with 4% paraformaldehyde (158127, Sigma–Aldrich) in D-PBS fixation solution under a 7° angle for 15 min. Next, the fixation solution was aspirated and chips were washed thrice by adding D-PBS and incubated under a 7° angle for 5 min. After washing, all chips were blocked by adding 5% goat serum (G6767, Sigma–Aldrich) in D-PBS blocking solution and incubating the OrganoPlate under a 7° angle for 30 min. Next, the blocking solution was aspirated and chips were incubated flat overnight at 4 °C with 25 µL biotinylated $\alpha_v\beta_3$ antibody (1:50 dilution, 304 412, BioLegend, San Diego, CA, USA) in the top channel in- and outlets and 15 µL in the bottom channel in- and outlets. A mouse biotinylated IgG1 isotype control antibody (1:50 dilution, 2 600 520, Sony Biotechnology, San Jose, CA, USA) was used to assess the specificity of the $\alpha_v\beta_3$ antibody. The next day, the antibody solution was aspirated and chips were washed thrice with 0.5% Tween-20 (P5927, Sigma–Aldrich) in D-PBS. After washing, all chips were blocked again using 5% goat serum in D-PBS under a 7° angle for 30 min. Then, chips were incubated in the dark with 25 µL of anti-mouse Alexa Fluor 488 antibody (1:100 dilution, A-11029, Invitrogen, Thermo Fisher Scientific) in the top channel in- and outlets and 15 µL in the bottom channel in- and outlets under a 7° angle at room temperature for 1 h. Next, chips were washed thrice with 0.5% Tween-20 in D-PBS, and 20 µg mL^{-1} Hoechst 33342 (H3570, Thermo Fisher Scientific) in D-PBS was added to all chips. After a 10 min incubation at room temperature in the dark under a 7° angle, the Hoechst 33342 solution was aspirated. Finally, 8 µL Vectashield (H-1400, Vector Laboratories Inc., Newark, CA, USA) was added to all channel inlets and incubated in the dark under a 7° angle for 15 min at room temperature. Thereafter, the plate was placed upside down and 3D z-stack images of 635 µm × 635 µm (512 × 512 pixels) with a z-step size of 0.8 µm were made using an A1R+ confocal microscope (Nikon Instruments, Amsterdam, the Netherlands) with a 20× water immersion objective (Cfi Apo LWD; numerical aperture 0.95; Nikon Instruments). Two laser channels and filter cubes were used: 1) Hoechst 33 342 excited at 405 nm and detected at 450/50 nm (center wavelength/bandwidth), and 2) Alexa Fluor 488 excited at 488 nm and detected at 525/50 nm.

Microbubble Preparation and Targeting: Lipid-coated MBs with a C_4F_{10} gas (F2 Chemicals, Preston, UK) core were produced using an indirect method with probe sonication for 1 min as previously described.[43,76] Briefly, the lipids were dissolved in an organic solvent (chloroform:methanol 9:1 volume ratio) and mixed to obtain a molar ratio of 84.8% DSPC (Lipoid, Ludwigshafen, Germany), 8.2% PEG40-stearate (Sigma–Aldrich), 5.9% DSPE-PEG2000, and 1.1% biotinylated DSPE-PEG2000 (both from Avanti Polar Lipids, Alabaster, AL, USA). Lipid films were created by drying the lipids using argon gas (Linde Gas Benelux, Schiedam, the Netherlands) for ≈15 min and freeze drying for 2 h using an Alpha 1–2 LD plus Freeze dryer (Martin Christ GmbH, Osterode am Harz, Germany). Lipid films were rehydrated in 5 mL C_4F_{10} saturated PBS and DiD (1,1′-dioctadecyl 3,3,3′,3′-tetramethylindodicarbocyanine perchlorate; D307, Thermo Fisher Scientific) lipid dye was added when

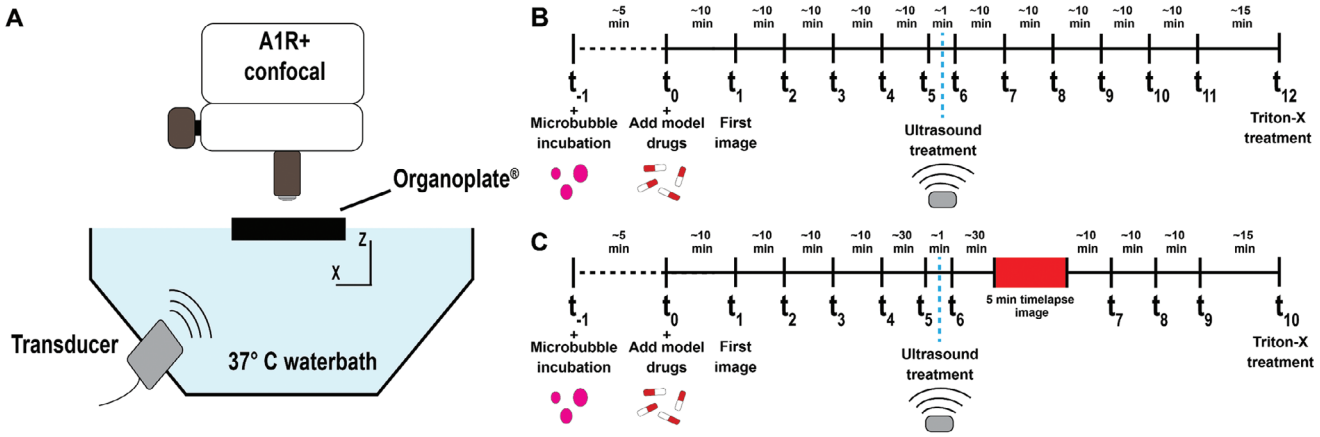

Figure 10. Imaging setup and experimental timeline for the barrier integrity (BI) assay. A) The optical imaging system allows for brightfield and epi-fluorescent microscopy imaging with a DS-Fi3 color camera (Nikon Instruments) and confocal microscopy imaging with the A1R+ scan head (Nikon Instruments). Ultrasound was applied under an angle of 45 ° in a 37 °C water bath underneath the OrganoPlate. B) Experimental timeline of the BI assay for all treatment conditions. C) The experimental timeline of BI assay includes 5 min timelapse image directly following treatment on a subset of treatment conditions. For both timelines, the $\alpha_V\beta_3$-targeted microbubbles were added at t_{-1} and the assays were started by adding the BI solution containing the model drugs at t_0.

fluorescent MBs were desired. The MBs were targeted to the $\alpha_v\beta_3$ integrin using biotin-streptavidin bridging as previously described.[62,77] Briefly, MBs were washed three to four times by centrifugation (400 g, 1 min, brake 9) using C_4F_{10}-saturated PBS until the subnatant was clear after which MBs were counted using a Coulter Counter Multisizer 3 (50 µm aperture tube, Beckman Coulter, Mijdrecht, the Netherlands). Next, $6{\cdot}10^8$ MBs were incubated on ice for 30 min with 60 µg streptavidin (S4762, Sigma–Aldrich). Subsequently, streptavidin-conjugated MBs were washed once by centrifugation and incubated with 6 µg biotin anti-human $\alpha_v\beta_3$ antibody (304412, BioLegend) on ice for 30 min. The $\alpha_v\beta_3$-tMBs were washed by centrifugation for one more time and the final $\alpha_v\beta_3$-tMB concentration was determined by counting using the Coulter Counter Multisizer 3.

To add the $\alpha_v\beta_3$-tMBs to the microvessels, they were diluted to a concentration of $1.5{\cdot}10^7$ $\alpha_v\beta_3$-tMBs mL^{-1} in 37 °C supplemented MCDB131 medium. Then, the plate was placed under an angle of 75° on the MIMETAS plate stand in such a way that the gel-cell interface layer was the highest point of the microvessel. While the plate was on the MIMETAS plate stand, 40 µL of the diluted $\alpha_v\beta_3$-tMBs solution was added to the top channel inlet and 30 µL to the top channel outlet, followed by a 5 min incubation step to allow the $\alpha_v\beta_3$-tMBs to bind to the cells in contact with the gel.

Experimental Setup: A custom-built Nikon A1R+ confocal microscopic setup was used to image the OrganoPlate (**Figure 10A**). This upright microscope was equipped with a DS-Fi3 (Nikon Instruments) color camera for brightfield and widefield fluorescence imaging, brightfield light source (Nikon Instruments), and metal halide light source (Fiber Illuminator Intensilight; Nikon Instruments). A V-shaped 37 °C water bath was placed underneath the microscope to allow for simultaneous temperature control of the OrganoPlate, microscopic imaging, and ultrasound insonification. A single element focused transducer (2.25 MHz center frequency; 76.2 mm focal length; −6 dB beam width at 2 MHz of 3 mm thus only covering one microvessel; V305; Panametrics-NDT, Olympus, Waltham, MA, USA) was positioned in the water bath under an incidence angle of 45° in relation to the OrganoPlate. The pressure output from the transducer was previously calibrated using a 1 mm needle hydrophone (Precision Acoustic, Dorchester, UK). The ultrasound focus was aligned to correspond with the optical focus of the microscope as previously described.[78] The 2 MHz frequency ultrasound waves were generated using an arbitrary waveform generator (33220A 20 MHz function, Agilent, Palo Alto, CA, USA) and amplified 50 dB (ENI 2100L, Electronics & Innovation, Rochester, NY, USA) to generate 100–850 kPa PNP in water and 90–750 kPa PNP in situ in the chips in the OrganoPlate.[33] Ultrasound was applied in 10 separate bursts of 10 or 1000 cycles per burst, which were applied every 3 s for a total of 30 s.

Barrier Integrity Assay: To assess the permeability of a microvessel-on-a-chip before and after different treatments, a BI assay was performed. The plate was divided into two sections and both sections were prepared and imaged separately to be able to achieve the desired imaging speed for the BI assay. The timeline of the BI assay is shown in Figure 10B. Following the 5 min $\alpha_v\beta_3$-tMB incubation (t_{-1}; see *Microbubble Preparation and Targeting*) in the vessel channel in the first section of the plate, all channels in section 1 were aspirated and the middle and bottom channels were wetted by adding 20 µL supplemented MCDB131 medium to the channel in- and outlet. A BI solution containing model drugs was prepared consisting of 0.5 mg mL^{-1} 150 kDa FITC dextran (46 946, Sigma–Aldrich) and 25 µg mL^{-1} propidium iodide (PI) (P4864, Sigma–Aldrich) in 37 °C supplemented MCDB131 medium. The BI assay was started by adding 40 µL BI solution to the top channel inlet and 30 µL to the top channel outlet (t_0) and placing the Organoplate in the 37 °C water bath (Figure 10A) with the inlet openings to the top. Using a 4× air objective (Cfi Plan Fluor, 17.2 mm working distance, Nikon Instruments), sequences of one brightfield and two fluorescent widefield images of 2880 µm × 2048 µm (2880 × 2048 pixels) were recorded ≈10 min apart with the DS-Fi3 color camera. The fluorescent BI solution was detected using the following excitation (Ex), dichroic mirror (DM), and emission (Em) filters: for FITC-dextran Ex469/35, DM497, and Em525/39; for PI Ex542/20, DM570, and Em620/52 (center wavelength/bandwidth in nanometers; Semrock Inc., Rochester, NY, USA). After adding the BI solution, the initial state of the microvessels was imaged for at least 30 min using five images (t_1–t_5), including an image just before treatment (t_5), to assess the permeability and quality of the microvessels. After the initial state, different treatments, depending on the conditions, were randomly applied for 30 s during which a brightfield video was made (≈2.5 frames per sec (fps)). In total 14 treatment conditions were investigated: ten different ultrasound plus $\alpha_v\beta_3$-tMB treatments and four controls (sham; tMBs only; 750 kPa 10 × 10 cycles ultrasound only; 750 kPa 10 × 1000 cycles ultrasound only). In addition, cell-free chips were included which contained no cells and only ECM gel. Directly after each treatment, another sequence of images was made (t_6). The sequence of imaging was continued for five more time points ≈10 min apart (t_7–t_{11}) for ≈45 min. Next, the barrier was disrupted by killing the cells to ensure that the observed permeability was a result of the cellular layer and not an artifact induced by for example liquid flow or the gel. To kill cells, Triton-X (T8787, Sigma–Aldrich) at a final concentration of 0.1% was added to all top channel inlets followed by one final sequence of

images (t_{12}). The above procedures were repeated for the second section of the plate starting at t_{-1}. In addition, a BI assay with a 5-min timelapse in brightfield and fluorescence directly following treatment was recorded (0.2 fps) for a subset of treatment conditions, see timeline in Figure 10C. In the initial state, i.e., up to t_5, and barrier disrupting step by killing cells (t_{10}), all procedures were identical as described above. However, here t_6 was the sequence of images directly before treatment. Directly after the 5 min timelapse, the sequence of imaging was continued for three more time points ≈10 min apart (t_7–t_9) for ≈45 min.

Live Cell 3D Imaging: Four days after cell seeding, live cell imaging was performed to quantify the number of bound $\alpha_v\beta_3$-tMBs in the microvessel and visualize sonoporation. The Organoplate was wetted and $\alpha_v\beta_3$-tMBs were incubated as described above (see *Microbubble Preparation and Targeting*). Staining solution with a final concentration of 20 µg mL^{-1} Hoechst 33342 (H3570, Thermo Fisher Scientific), 12 µg mL^{-1} CellMask Green Plasma Membrane Stain (C37608, Thermo Fisher Scientific), and 25 µg mL^{-1} Propidium Iodide (PI) was prepared in 37 °C supplemented MCDB131 medium. Next, a staining solution was added for the BI solution described above in the BI assay section. Following incubation, the plate was imaged upside down such that the microvessels were within the working distance of the Cfi Apo LWD 20× water immersion objective (Nikon Instruments). Sixteen 3D z-stack images of 635 µm × 635 µm (512 × 512 pixels) with a z-step size of 0.8 µm were made in eight different microvessels using an A1R+ confocal microscope (Nikon Instruments). Four laser channels and filter cubes were used: 1) Hoechst 44 332 excited at 405 nm and detected at 450/50 nm (center wavelength/bandwidth), 2) CellMask Green Plasma Membrane Stain excited at 488 nm and detected at 525/50 nm, 3) PI excited at 561 nm and detected at 595/50 nm, 4) DiD excited at 640 nm and detected at 700/75 nm. Channel 1 and 4 were excited and detected simultaneously because there is no spectral overlap between Hoechst 44332 and DiD. Next, the Organoplate was placed back into the original position with the bottom of the plate inside the water bath, and ultrasound was applied as described above. After treatment, the Organoplate was positioned upside down again and the microvessels were imaged once more which was 14–70 min after treatment.

Microvessel Viability Protocol: To investigate whether the treatment conditions affected cell viability on a microvessel scale, the viability of the cells within the entire microvessel was assessed using a WST-8 chromatography assay. The BI assay up to timepoint t_6 was performed as described above and illustrated in Figure 10B. At timepoint t_6 of the BI assay, the Organoplate was taken out of the imaging setup and 0.1% Triton-X (final concentration; T8787, Sigma–Aldrich) was added to the desired chips and incubated for 10 min at 37 °C. Next, all chips were aspirated and 25 µL of WST-8 working solution was added to the top and bottom channel in- and outlets. The WST-8 working solution was made by diluting the WST-8 stock solution (96992, Sigma–Aldrich) 1:11 in a supplemented MCDB131 medium. Next, the Organoplate was incubated for 30 min on the OrganoFlow rocker as described above. This was followed by placing the Organoplate flat for 5 min to stop the flow. Subsequently, the absorbance at a wavelength of 450 nm was measured in the in- and outlets of the top channel using a spectrophotometer (Spectramax iD3, Molecular Devices, LLC, San Jose, CA, USA). The average time elapsed between the last treatment and the absorbance reading was 78 min (range 73–83 min). The negative controls were: MCDB131 medium without WST-8 reagent and three cell-free conditions with WST-8 reagent of which one was treated with $\alpha_v\beta_3$-tMBs only and one with ultrasound (750 kPa 10 × 1000 cycles) plus $\alpha_v\beta_3$-tMBs. The positive control was the microvessels incubated with 0.1% Triton-X as described above, which kills all the cells.

Nuclei and Bound $\alpha_v\beta_3$-tMB Quantification Analysis: Live cell 3D stack images were divided into three segments: 1) the bottom of the microvessel, i.e., the 2D cell layer at the bottom of the Organoplate up to the top of the phaseguide; 2) the gel-cell interface; and 3) the top of the microvessel, i.e., the 2D cell layer on the top of the microvessel. Nuclei were counted using the "Object Analyzer" with a watershed segmentation of 30% in the Huygens Professional image analysis software (Scientific Volume Imaging, Hilversum, the Netherlands). Microbubbles were counted using the "Small particles geometry" analysis with a watershed segmentation of 10% in the Huygens software. To separate $\alpha_v\beta_3$-tMB clusters into individual microbubbles, the Coulter Counter Multisizer 3 measurements were used. Particles were classified as debris when the particle volume was below the *d*10%, (2.1 µm;, i.e., the $\alpha_v\beta_3$-tMB diameter below which 10% of the cumulative amount of $\alpha_v\beta_3$-tMBs was found), classified as one $\alpha_v\beta_3$-tMB when the particle volume was between the *d*10% and *d*90% (6.5 µm; i.e., the tMB diameter below which 90% of the cumulative amount of $\alpha_v\beta_3$-tMBs was found) or classified as multiple $\alpha_v\beta_3$-tMBs when the particle volume was above the *d*90%. When classified as multiple $\alpha_v\beta_3$-tMBs, the particle volume was divided by the mean voxel volume (i.e., 18 voxels) of one $\alpha_v\beta_3$-tMB (i.e., mean $\alpha_v\beta_3$-tMB diameter of 4.0 µm) and all decimal values were rounded up to calculate the number of single $\alpha_v\beta_3$-tMBs in the multiple particles. The polydispersity of the $\alpha_v\beta_3$-tMB was assessed by the SPAN, defined as (d90%–d10%)/d50% where d90%, d10%, and d50% were the microbubble diameters below which 90, 10, and 50% of the cumulative amount of microbubbles were found.

Data Analysis BI Assay: All data analysis was performed using MATLAB R2021b (The MathWorks Inc., Natick, MA, USA). Leakage was quantified by drawing a region of interest (ROI) in the top microvessel and middle gel channels and measuring the average pixel intensity of the green FITC-dextran signal per ROI. The leakage percentage over time was calculated by dividing the fluorescent intensity of the middle gel channel ROI (I_{gel}) by the intensity of the top microvessel channel ROI (I_{ves}):

$$\text{Equation Leakage percentage} = \frac{I_{gel}}{I_{ves}} \cdot 100 \quad (1)$$

If the leakage value exceeded 50% within the first 30 min of the BI assay, the microvessels were deemed unsuitable for the assay and excluded. The Apparent Permeability (P_{app}) of the vessels was calculated in the initial state (i.e., before treatment) and after treatment using the Excel solver tool provided by Mimetas.[79] For the BI assay with the 5 min timelapse (as illustrated in Figure 10C), the P_{app} was also calculated for the 5 min period directly following the ultrasound treatment.

Data Analysis Sonoporation: All data analysis was performed using MATLAB R2021b (The MathWorks Inc.). Sonoporation was quantified by drawing an ROI of 150 µm in the y-direction on the gel-cell interface part of the top microvessel channel and measuring the average PI signal intensity per ROI. As the microscopy imaging was done from above, this ROI also included half of the cells at the bottom of the microvessel. Consequently, ≈50% of the total vessel surface was within the ROI. The percentage increase in PI signal was calculated using the following formula: $(PI_{t6} - PI_{t5})/PI_{t5} \times 100\%$, where PI_{t5} is the signal in the last image before treatment and PI_{t6} the first image after treatment. Image t_6 was always taken within 45 s after the last ultrasound pulse. These time points relate to the timeline illustrated in Figure 10B.

Data Analysis: $\alpha_v\beta_3$-tMB Displacement, $\alpha_v\beta_3$-tMB Clustering and Relation with Vascular Permeability/PI Uptake in vessel segments: $\alpha_v\beta_3$-tMB displacement and clustering were extracted from the brightfield videos recorded during ultrasound treatment and analyzed with MATLAB R2019a (The MathWorks Inc.). First, the videos were denoised using a Gaussian filter and cropped so only the top microvessel channel was imaged. Second, the difference in pixel intensity before and after each ultrasound pulse was analyzed. Since $\alpha_v\beta_3$-tMB scatter light and scattering effectively decreases the light that reaches the sensor, $\alpha_v\beta_3$-tMB displacement will lead to a pixel intensity increase at the position where the $\alpha_v\beta_3$-tMB displaced from. Therefore, $\alpha_v\beta_3$-tMB displacement was quantified as the cumulative pixel intensity increase between frames. An $\alpha_v\beta_3$-tMB cluster was defined as a group of at least 40 pixels (40 µm^2, i.e., 3.3 times the mean $\alpha_v\beta_3$-tMB area) with an intensity decrease, discarding those intersecting the boundaries of the cropped vessel. To reject noise in both the pixel intensity increase and decrease, only intensity changes above a heuristic threshold determined from the control recordings were considered. The distance between $\alpha_v\beta_3$-tMB clusters was obtained using the MATLAB built-in pdist function.

The relation between $\alpha_v\beta_3$-MB clusters and $\alpha_v\beta_3$-MB displacement, vascular permeability increase, and PI increase was locally assessed. For this, the recording of the fluorescent channels before and after ultrasound treatment was loaded into MATLAB R2021b (The MathWorks Inc.) and

filtered with a 2D wiener filter. The vascular permeability increase was measured on the middle gel channel, whereas the PI increase was measured on the top microvessel channel. In order to obtain spatial information, 200 µm wide segments were defined along the x-direction of the ROI (see red-dotted rectangles in Figure 6A), measuring the number of $\alpha_v\beta_3$-tMB clusters, cumulative $\alpha_v\beta_3$-tMB displacement, vascular permeability increase, and PI increase in each segment. Increases in vascular permeability and PI were only considered relevant if they exceeded a threshold, i.e., 0.01 A.U. for local leakage and 0.005 A.U. for local PI increase, which was defined as the quantile 96 value from the segments belonging to the control-treated microvessels (Figure S8, Supporting Information).

Statistical Analysis: All statistical analysis was performed in SPSS (IBM, Armonk, NY, USA). The Shapiro-Wilk test of normality was used to assess whether data were parametric or non-parametric. For non-parametric data, the Mann–Whitney U test was used while parametric data was tested for equality of variances using Levene's test after which a student's *t*-test was used for data with equal variances or the Welch's *t*-test for data with unequal variances. Reported p-values are two-tailed and $p < 0.05$ is indicated with *,$p < 0.01$ is indicated with **, and $p < 0.001$ is indicated with ***. In all Figures, except for Figure 9, the indicated significance represents changes compared to the four control conditions (i.e., sham, $\alpha_v\beta_3$-tMBs only, and ultrasound only (750 kPa 10 × 10 cycles and 750 kPa and 10 × 1000 cycles) and the differences within these significant groups. In Figure 9, the indicated significance represented the differences compared to the one positive and four negative control conditions. Pearson's correlation was performed on all data points above the control threshold in Figure 8 using Graphpad Prism 9 (Dotmatics, Boston, MA, USA).

Supporting Information

Supporting Information is available from the Wiley Online Library or from the author.

Acknowledgements

This work was funded in majority by the Applied and Engineering Sciences (TTW) (Vidi-project 17543), part of the Dutch Research Council NWO, awarded to K.K. J.C. and G.H.K. gratefully acknowledge financial support from the Dutch Research Council NWO (project number VI.C.182.004 of the NWO Talent Programme). The authors would like to thank Robert Beurskens, Phoei Ying Tang, and Cheryl Mok from the Biomedical Engineering of the Department of Cardiology, Michiel Manten from the Department of Experimental Medical Instrumentation, and Marcel Sluijter from the Laboratory of Paediatrics, all from Erasmus MC, the Netherlands, for technical assistance.

Conflict of Interest

Kristina Bishard and Sebastiaan J. Trietsch are employees of MIMETAS BV, which is marketing the OrganoPlate and Sebastiaan J. Trietsch is a shareholder of MIMETAS BV. OrganoPlate is a registered trademark of MIMETAS BV. The other authors declare no conflict of interest.

Data Availability Statement

The data that support the findings of this study are available from the corresponding author upon reasonable request.

Keywords

microbubbles, Microvessel-on-a-chip, sonoporation, ultrasound, vascular permeability

Received: August 26, 2024
Revised: October 29, 2024
Published online:

[1] A. A. Van der Veldt, M. Lubberink, I. Bahce, M. Walraven, M. P. de Boer, H. N. Greuter, N. H. Hendrikse, J. Eriksson, A. D. Windhorst, P. E. Postmus, H. M. Verheul, E. H. Serne, A. A. Lammertsma, E. F. Smit, *Cancer Cell* **2012**, *21*, 82.
[2] S. Heskamp, O. C. Boerman, J. D. Molkenboer-Kuenen, W. J. Oyen, W. T. van der Graaf, H. W. van Laarhoven, *Int. J. Cancer* **2013**, *133*, 307.
[3] M. Arjaans, T. H. Oude Munnink, S. F. Oosting, A. G. Terwisscha van Scheltinga, J. A. Gietema, E. T. Garbacik, H. Timmer-Bosscha, M. N. Lub-de Hooge, C. P. Schroder, E. G. de Vries, *Cancer Res.* **2013**, *73*, 3347.
[4] K. Kooiman, S. Roovers, S. A. G. Langeveld, R. T. Kleven, H. Dewitte, M. A. O'Reilly, J. M. Escoffre, A. Bouakaz, M. D. Verweij, K. Hynynen, I. Lentacker, E. Stride, C. K. Holland, *Ultrasound Med Biol* **2020**, *46*, 1296.
[5] J. Deprez, G. Lajoinie, Y. Engelen, S. C. De Smedt, I. Lentacker, *Adv Drug Deliv Rev* **2021**, *172*, 9.
[6] S. R. Wilson, P. N. Burns, Y. Kono, *Ultrasound Med Biol* **2020**, *46*, 1059.
[7] T. R. Porter, S. B. Feinstein, F. J. Ten Cate, A. E. van den Bosch, *Ultrasound Med Biol* **2020**, *46*, 1071.
[8] B. Helfield, X. Chen, S. C. Watkins, F. S. Villanueva, *Proc Natl Acad Sci U S A* **2016**, *113*, 9983.
[9] I. Beekers, M. Vegter, K. R. Lattwein, F. Mastik, R. Beurskens, A. F. W. van der Steen, N. de Jong, M. D. Verweij, K. Kooiman, *J. Controlled Release* **2020**, *322*, 426.
[10] B. D. Meijering, L. J. Juffermans, A. van Wamel, R. H. Henning, I. S. Zuhorn, M. Emmer, A. M. Versteilen, W. J. Paulus, W. H. van Gilst, K. Kooiman, N. de Jong, R. J. Musters, L. E. Deelman, O. Kamp, *Circ. Res.* **2009**, *104*, 679.
[11] B. Meijlink, H. R. van der Kooij, Y. Wang, H. Li, S. Huveneers, K. Kooiman, *J. Controlled Release* **2024**, *376*, 1176.
[12] K. Kooiman, H. J. Vos, M. Versluis, N. de Jong, *Adv. Drug Delivery Rev.* **2014**, *72C*, 28.
[13] J. Park, Z. Fan, C. X. Deng, *J. Biomech.* **2011**, *44*, 164.
[14] R. E. Kumon, M. Aehle, D. Sabens, P. Parikh, Y. W. Han, D. Kourennyi, C. X. Deng, *Ultrasound Med Biol* **2009**, *35*, 494.
[15] Z. Fan, H. Liu, M. Mayer, C. X. Deng, *Proc Natl Acad Sci U S A* **2012**, *109*, 16486.
[16] I. Beekers, F. Mastik, R. Beurskens, P. Y. Tang, M. Vegter, A. F. W. van der Steen, N. de Jong, M. D. Verweij, K. Kooiman, *Ultrasound in Med. Biol.* **2020**, *46*, 2017.
[17] I. Beekers, S. A. G. Langeveld, B. Meijlink, A. F. W. van der Steen, N. de Jong, M. D. Verweij, K. Kooiman, *J Control Release* **2022**, *347*, 460.
[18] B. Helfield, X. Chen, S. C. Watkins, F. S. Villanueva, *Ultrasound Med Biol* **2020**, *46*, 1686.
[19] S. V. Morse, A. N. Pouliopoulos, T. G. Chan, M. J. Copping, J. Lin, N. J. Long, J. J. Choi, *Radiology* **2019**, *291*, 459.
[20] S. M. Stieger, C. F. Caskey, R. H. Adamson, S. Qin, F. R. Curry, E. R. Wisner, K. W. Ferrara, *Radiology* **2007**, *243*, 112.
[21] M. Amate, J. Goldgewicht, B. Sellamuthu, J. Stagg, F. T. H. Yu, *Nanotheranostics* **2020**, *4*, 256.
[22] F. Vlachos, Y. S. Tung, E. Konofagou, *Magn Reson Med* **2011**, *66*, 821.
[23] P. T. Yemane, A. K. O. Aslund, S. Snipstad, A. Bjorkoy, K. Grendstad, S. Berg, Y. Morch, S. H. Torp, R. Hansen, C. L. Davies, *Ultrasound Med Biol* **2019**, *45*, 3028.
[24] G. Dimcevski, S. Kotopoulis, T. Bjanes, D. Hoem, J. Schjott, B. T. Gjertsen, M. Biermann, A. Molven, H. Sorbye, E.

McCormack, M. Postema, O. H. Gilja, *J Control Release* **2016**, *243*, 172.
[25] S. Roovers, T. Segers, G. Lajoinie, J. Deprez, M. Versluis, S. C. De Smedt, I. Lentacker, *Langmuir* **2019**, *35*, 10173.
[26] G. Lajoinie, I. De Cock, C. C. Coussios, I. Lentacker, S. L. Gac, E. Stride, M. Versluis, *Biomicrofluidics* **2016**, *10*, 011501.
[27] E. Memari, F. Hui, H. Yusefi, B. Helfield, *J Control Release* **2023**, *358*, 333.
[28] A. Pollet, J. M. J. den Toonder, *Bioengineering (Basel)* **2020**, *7*, 17.
[29] E. K. Juang, I. De Cock, C. Keravnou, M. K. Gallagher, S. B. Keller, Y. Zheng, M. Averkiou, *Langmuir* **2019**, *35*, 10128.
[30] G. Silvani, C. Scognamiglio, D. Caprini, L. Marino, M. Chinappi, G. Sinibaldi, G. Peruzzi, M. F. Kiani, C. M. Casciola, *Small* **2019**, *15*, e1905375.
[31] S. J. Trietsch, E. Naumovska, D. Kurek, M. C. Setyawati, M. K. Vormann, K. J. Wilschut, H. L. Lanz, A. Nicolas, C. P. Ng, J. Joore, S. Kustermann, A. Roth, T. Hankemeier, A. Moisan, P. Vulto, *Nat. Commun.* **2017**, *8*, 262.
[32] L. de Haan, J. Suijker, R. van Roey, N. Berges, E. Petrova, K. Queiroz, W. Strijker, T. Olivier, O. Poeschke, S. Garg, L. J. van den Broek, *Int. J. Mol. Sci.* **2021**, *22*, 8234.
[33] I. Beekers, T. van Rooij, M. D. Verweij, M. Versluis, N. de Jong, S. J. Trietsch, K. Kooiman, *IEEE Trans Ultrason Ferroelectr Freq Control* **2018**, *65*, 570.
[34] S. A. G. Langeveld, B. Meijlink, K. Kooiman, *Curr. Opin. Chem. Biol.* **2021**, *63*, 171.
[35] T. van Rooij, I. Skachkov, I. Beekers, K. R. Lattwein, J. D. Voorneveld, T. J. A. Kokhuis, D. Bera, Y. Luan, A. F. W. van der Steen, N. de Jong, K. Kooiman, *J Control Release* **2016**, *238*, 197.
[36] K. Kooiman, M. Emmer, M. Foppen-Harteveld, A. van Wamel, N. de Jong, *IEEE Trans. Biomed. Eng.* **2010**, *57*, 29.
[37] P. Karki, A. A. Birukova, *Pulm Circ* **2018**, *8*, 1.
[38] N. Fekete, A. V. Beland, K. Campbell, S. L. Clark, C. A. Hoesli, *Transfusion* **2018**, *58*, 1800.
[39] J. Liu, H. Zheng, P. S. Poh, H. G. Machens, A. F. Schilling, *Int. J. Mol. Sci.* **2015**, *16*, 15997.
[40] K. E. Sung, G. Su, C. Pehlke, S. M. Trier, K. W. Eliceiri, P. J. Keely, A. Friedl, D. J. Beebe, *Biomaterials* **2009**, *30*, 4833.
[41] V. van Duinen, W. Stam, V. Borgdorff, A. Reijerkerk, V. Orlova, P. Vulto, T. Hankemeier, A. J. van Zonneveld, *J Vis Exp* **2019**, e59678.
[42] A. G. Monteduro, S. Rizzato, G. Caragnano, A. Trapani, G. Giannelli, G. Maruccio, *Biosens. Bioelectron.* **2023**, *231*, 115271.
[43] S. A. G. Langeveld, B. Meijlink, I. Beekers, M. Olthof, A. F. W. van der Steen, N. de Jong, K. Kooiman, *Pharmaceutics* **2022**, *14*, 311.
[44] E. A. Jaffe, *Human Pathology* **1987**, *18*, 234.
[45] V. van Duinen, A. van den Heuvel, S. J. Trietsch, H. L. Lanz, J. M. van Gils, A. J. van Zonneveld, P. Vulto, T. Hankemeier, *Sci. Rep.* **2017**, *7*, 18071.
[46] A. Nicolas, F. Schavemaker, K. Kosim, D. Kurek, M. Haarmans, M. Bulst, K. Lee, S. Wegner, T. Hankemeier, J. Joore, K. Domansky, H. L. Lanz, P. Vulto, S. J. Trietsch, *Lab Chip* **2021**, *21*, 1676.
[47] X. Zhao, C. Pellow, D. E. Goertz, *Theranostics* **2023**, *13*, 250.
[48] C. K. Holland, C. X. Deng, R. E. Apfel, J. L. Alderman, L. A. Fernandez, K. J. Taylor, *Ultrasound Med Biol* **1996**, *22*, 917.
[49] T. Nhan, A. Burgess, E. E. Cho, B. Stefanovic, L. Lilge, K. Hynynen, *J. Controlled Release* **2013**, *172*, 274.
[50] D. H. Thomas, V. Sboros, M. Emmer, H. Vos, N. de Jong, *IEEE Trans Ultrason Ferroelectr Freq Control* **2013**, *60*, 105.
[51] C. F. Caskey, S. M. Stieger, S. Qin, P. A. Dayton, K. W. Ferrara, *J Acoust Soc Am* **2007**, *122*, 1191.
[52] T. Frey, *Cytometry* **1995**, *21*, 265.
[53] W. D. Wilson, C. R. Krishnamoorthy, Y. H. Wang, J. C. Smith, *Biopolymers* **1985**, *24*, 1941.
[54] Y. Hu, J. M. Wan, A. C. Yu, *Ultrasound Med Biol* **2013**, *39*, 2393.
[55] I. De Cock, E. Zagato, K. Braeckmans, Y. Luan, N. de Jong, S. C. De Smedt, I. Lentacker, *J Control Release* **2015**, *197*, 20.
[56] T. J. Kokhuis, V. Garbin, K. Kooiman, B. A. Naaijkens, L. J. Juffermans, O. Kamp, A. F. van der Steen, M. Versluis, N. de Jong, *Ultrasound Med Biol* **2013**, *39*, 490.
[57] V. Garbin, M. Overvelde, B. Dollet, N. de Jong, D. Lohse, M. Versluis, *Phys Med Biol* **2011**, *56*, 6161.
[58] X. Chen, J. Wang, J. J. Pacella, F. S. Villanueva, *Ultrasound Med Biol* **2016**, *42*, 528.
[59] A. A. Doinikov, *Bubble and ParticleDynamics in Acoustic Fields: Modern Trends and Applications*, ResearchSignpost, Trivandrum, Kerala, India **2005**, pp. 95–143.
[60] S. Kotopoulis, M. Postema, *Ultrasonics* **2010**, *50*, 260.
[61] C. Lazarus, A. N. Pouliopoulos, M. Tinguely, V. Garbin, J. J. Choi, *J Acoust Soc Am* **2017**, *142*, 3135.
[62] I. Skachkov, Y. Luan, A. F. van der Steen, N. de Jong, K. Kooiman, *IEEE Trans Ultrason Ferroelectr Freq Control* **2014**, *61*, 1661.
[63] T. J. A. Kokhuis, B. A. Naaijkens, L. J. M. Juffermans, O. Kamp, A. F. W. van der Steen, M. Versluis, N. de Jong, *Appl. Phys. Lett.* **2017**, *111*, 023701.
[64] C. Pellow, M. A. O'Reilly, K. Hynynen, G. Zheng, D. E. Goertz, *Nano Lett.* **2020**, *20*, 4512.
[65] D. Gonzalez-Rodriguez, C. Morel, E. Lemichez, *Adv. Exp. Med. Biol.* **2020**, *1267*, 101.
[66] L. Claesson-Welsh, E. Dejana, D. M. McDonald, *Trends Mol. Med.* **2021**, *27*, 314.
[67] L. Boyer, A. Doye, M. Rolando, G. Flatau, P. Munro, P. Gounon, R. Clement, C. Pulcini, M. R. Popoff, A. Mettouchi, L. Landraud, O. Dussurget, E. Lemichez, *J. Cell Biol.* **2006**, *173*, 809.
[68] J. T. Belcik, B. P. Davidson, A. Xie, M. D. Wu, M. Yadava, Y. Qi, S. Liang, C. R. Chon, A. Y. Ammi, J. Field, L. Harmann, W. M. Chilian, J. Linden, J. R. Lindner, *Circulation* **2017**, *135*, 1240.
[69] N. Rong, M. Zhang, Y. Wang, H. Wu, H. Qi, X. Fu, D. Li, C. Yang, Y. Wang, Z. Fan, *Ultrason. Sonochem.* **2020**, *67*, 105125.
[70] D. R. Green, *Cell* **2005**, *121*, 671.
[71] C. D. Ohl, M. Arora, R. Ikink, N. de Jong, M. Versluis, M. Delius, D. Lohse, *Biophys. J.* **2006**, *91*, 4285.
[72] S. J. Trietsch, G. D. Israels, J. Joore, T. Hankemeier, P. Vulto, *Lab Chip* **2013**, *13*, 3548.
[73] P. Vulto, S. Podszun, P. Meyer, C. Hermann, A. Manz, G. A. Urban, *Lab Chip* **2011**, *11*, 1596.
[74] M. K. Vormann, L. Gijzen, S. Hutter, L. Boot, A. Nicolas, A. van den Heuvel, J. Vriend, C. P. Ng, T. T. G. Nieskens, V. van Duinen, B. de Wagenaar, R. Masereeuw, L. Suter-Dick, S. J. Trietsch, M. Wilmer, J. Joore, P. Vulto, H. L. Lanz, *AAPS J.* **2018**, *20*, 90.
[75] N. L. G. Mattei, E. J. Breel, *Optics11 White Paper* **2017**, *1*, 1.
[76] S. A. G. Langeveld, C. Schwieger, I. Beekers, J. Blaffert, T. van Rooij, A. Blume, K. Kooiman, *Langmuir* **2020**, *36*, 3221.
[77] K. Kooiman, M. Foppen-Harteveld, A. F. van der Steen, N. de Jong, *J Control Release* **2011**, *154*, 35.
[78] I. Beekers, K. R. Lattwein, J. J. P. Kouijzer, S. A. G. Langeveld, M. Vegter, R. Beurskens, F. Mastik, R. Verduyn Lunel, E. Verver, A. F. W. van der Steen, N. de Jong, K. Kooiman, *Ultrasound Med Biol* **2019**, *45*, 2575.
[79] C. Soragni, T. Vergroesen, N. Hettema, G. Rabussier, H. L. Lanz, S. J. Trietsch, L. J. de Windt, C. P. Ng, *STAR Protoc* **2023**, *4*, 102051.